N O T I C E

THIS DOCUMENT HAS BEEN REPRODUCED FROM
MICROFICHE. ALTHOUGH IT IS RECOGNIZED THAT
CERTAIN PORTIONS ARE ILLEGIBLE, IT IS BEING RELEASED
IN THE INTEREST OF MAKING AVAILABLE AS MUCH
INFORMATION AS POSSIBLE

Contract NAS9-16055

A THEORETICAL STUDY OF MICROWAVE BEAM ABSORPTION BY A RECTENNA

FINAL REPORT

Prepared For:

National Aeronautics and Space Administration
Lyndon B. Johnson Space Center

Prepared by:

James H. Ott
James S. Rice
Donald C. Thorn

January 14, 1981

Novar Electronics Corporation
24 Brown Street
Barberton, Ohio 44203

NOVAR

Contract NAS9-16055

A THEORETICAL STUDY OF MICROWAVE BEAM ABSORPTION BY A RECTENNA

FINAL REPORT

Prepared For:

National Aeronautics and Space Administration
Lyndon B. Johnson Space Center

Prepared by:

James H. Ott
James S. Rice
Donald C. Thorn

January 14, 1981

Novar Electronics Corporation
24 Brown Street
Barberton, Ohio 44203

TABLE OF CONTENTS

APPENDIXES

iv

FIGURES

TABLE

A THEORETICAL STUDY OF MICROWAVE BEAM

ABSORPTION BY A RECTENNA -- FINAL REPORT

INTRODUCTION

A workable Satellite Power System will require efficient transmission and reception of an environmentally benign microwave beam. The object of Novar Electronics Corporation's work as defined in Task IJ, Contract NAS9-10655 has been to establish theoretical operational parameters for an SPS Rectenna. Such parameters provide understanding of the Reference Design Rectenna as well as insights for possible improvements.

Specifically, Novar studied:

1. The conditions required for a large Rectenna array (i.e., Reference Design) to absorb nearly 100% of transmitted energy;

2. Design parameters, including element spacing, and the manner in which these affect scatter;

3. Amplitudes and directions of scatter and development of strategies for mitigation;

4. Effects on Rectenna behavior of external factors such as weather and aircraft overflights.

This report details the methods of Novar's investigation, results, inferences, and recommendations for follow-up studies.

SUMMARY

Establishment of theoretical operating parameters for the SPS Rectenna required four investigative phases: (1) a search of the literature of antenna theory and application; (2) development of models capable of generating operational data; (3) analyses of these data; and (4) evaluation of the effects of some types of external factors which interfere with reception of the microwave beam. Novar developed two models descriptive of the microwave absorption process: the Current Sheet Model (CSM) and the Waveguide Model (WGM). Derived from Maxwell's equations for plane waves, these models made possible the quantification of Rectenna absorption characteristics and prediction of conditions necessary for total absorption of a microwave beam. Effects of aircraft overflight of a rectenna were also confirmed experimentally.

RESULTS

Novar's studies have produced theoretical bases for predicting Rectenna efficiency, operational characteristics, control cf spurious reradiation, and the potential for certain design modifications to permit more efficient functioning of Rectenna elements as well as substantial savings in construction costs.

Specifically, Novar's analyses indicate that:

1. Nearly 100% absorption of an incident power beam (i.e., zero scatter) can be predicted under certain idealizations for an SPS power beam either

    a. Perpendicular to the Reference Design Rectenna, or

    b. Off-normal incidence;

2. Overflights of the Rectenna can induce localized signal surges which can be quite large.

3. Certain deviations from ideal conditions can produce specular and grating-lobe scatter. Some of these deviations have been characterized to provide insights into their prevention and/or mitigation.

CONCLUSIONS

1. A Rectenna of reference design is capable of nearly 100% absorption of a perpendicularly incident planar beam;

2. Greater separation of dipole-diode elements (to somewhat under 1.15λ as opposed to 0.6λ in Reference Design) would result in higher efficiency per element as well as substantial reduction in the number of elements required;

3. Prediction of 100% absorption at off-normal angles of incidence argues the feasibility of a flat or terrain-conforming Rectenna. Such a configuration would have several advantages over the Reference Design, especially in construction and maintenance;

4. Because certain accidental conditions would induce momentary power-surges, Rectenna elements must be designed and manufactured to tolerate transient overloads;

5. Power levels and hence beam position must be tightly controlled in order to maintain the impedance stability necessary for total energy absorption.

RECOMMENDATIONS AND SUGGESTIONS

1. Although Novar has been able to obtain preliminary measurements of certain atmospheric influences on Rectenna operation, it is quite apparent that

more work is needed. As discussed below and in the Appendixes, ideal functioning of the Rectenna depends upon ideal behavior of the incoming beam. Errors due to deviations in arrival angle (azimuth or elevation) for the entire plane-wave are readily estimated (see page 14). Scattering resulting from non-plane waves (due to atmospheric effects) can be evaluated (see Appendix E) only to the extent that the nature of these non-plane waves can be accurately estimated. Further, misformation or misaiming of the power beam due to atmospheric phenomena would cause excursions from normal Rectenna behavior. Rectenna elements lack the aperture averaging associated with most large antennas and the incident signal will be unmodulated. An examination of the available literature has failed to yield data for propagation under these conditions. Therefore, a series of propagation experiments should be designed and executed (including those in Appendix F) to support the Rectenna design by providing data for system evaluation.

2. A Rectenna test panel should be constructed with adjustable elements. Such a test panel would provide an experimental facility for:

        a. Measuring effects of spacing and geometric configuration and

        b. Demonstrating total absorption capability for off-normal incidence.

3. Grating lobe analysis (Appendix D) should be extended beyond the work reported here:

a. For the "billboard" (Reference Design) Rectenna, edge-scatter and extra grating lobes due to this configuration should be evaluated;

b. For the "terrain-conforming" design suggested here (page 11), a more rigorous analysis of grating lobes at both fundamental and harmonic frequencies should be u..dertaken. We know from developments in Appendix D that grating lobes can occur under certain conditions and how they can be avoided in certain simple cases. The directions, magnitudes, and beam-widths of some of these lobes depend upon information not yet fully established (or available to us). If a full analysis of grating lobe behavior is deemed necessary, the approach taken in Appendix D can be extended.

4. Rectenna element impedance, critical to total absorption, is probably a strong function of power level. Since the incident beam is planned to have a Gaussian distribution, beam pointing errors may produce serious consequences. An effort should be made to fully define element impedance variations caused by non-linearity of the diode.

TECHNICAL DISCUSSION

The Reference Design Rectenna (Figure 1) represents the present stage of a technology pioneered by W. C. Brown[1,2] of Raytheon and R. M. Dickinson[3] of JPL. Both have reported microwave-to-dc conversion efficiencies exceeding 80% with

experimental arrays. However, because of a frequently-expressed concern over lack of theoretical rationale for efficiencies above 50% and because of the size and scope of the SPS program,
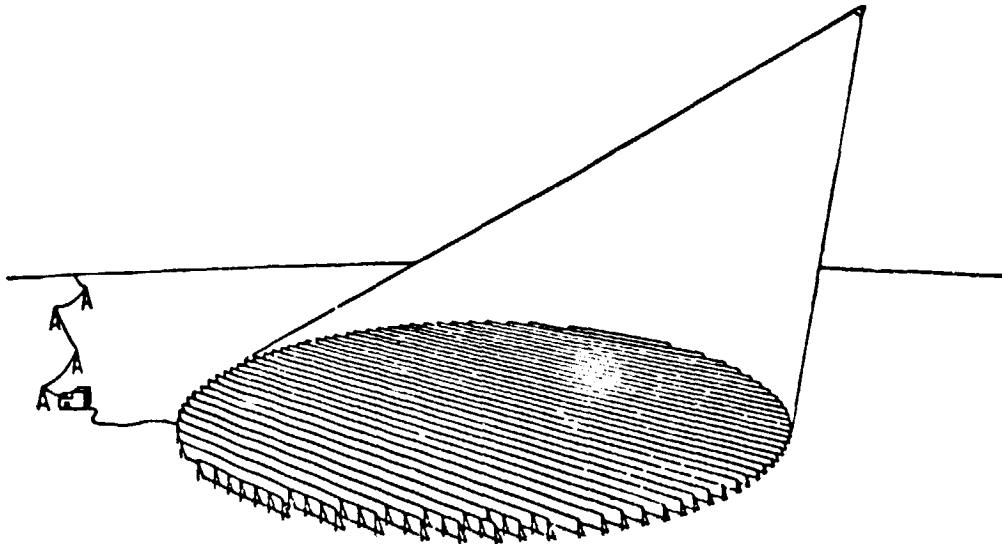
FIGURE 1

REFERENCE DESIGN "BILLBOARD" RECTENNA

Novar Electronics Corporation undertook to develop models descriptive of the absorption characteristics of individual elements in a large planar Rectenna array. The two models developed for this study are the Current Sheet Model (CSM) and the Waveguide Model (WGM). Both models are premised on the assumption, drawn from our own experience and that

of others[4], that a very large finite Rectenna array can be closely approximated by a infinite array.*

CURRENT SHEET MODEL (CSM)

The CSM, developed in Appendix B from bases developed in Appendix A, is based upon the current-sheet equivalency of a large planar array above a reflector (Figure 2). The current sheet has those properties of resistive absorbers
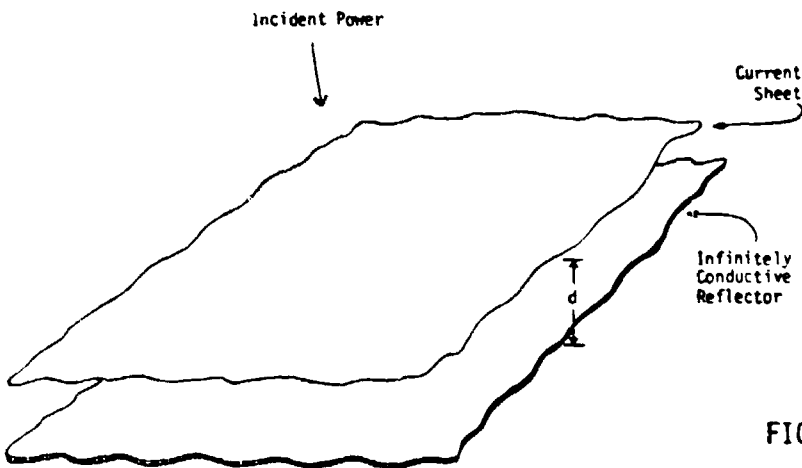
FIGURE 2

CURRENT SHEET MODEL

described by Jasik[5] and Kraus[6]. The model is characterized by an expression for the fraction of an incident plane-wave reflected from the sheet (assuming infinite extent). The work of Wait[7,8] indicates that a current sheet having

---

*The rate of change in power density at the Rectenna is so small that when any given dipole is excited the dipoles in all directions near enough to have significant interaction appear to be identically excited.

uniformly distributed currents can effectively model the discrete-dipole array of the Reference Model (see below and Appendix C). When Rectenna elements are sufficiently close, field components other than the plane-wave are evanescent (reactive), near-field components which become negligible at any significant distance from the array. For the present discussion, element spacing is small enough and the Rectenna large enough to justify the model.

From Maxwell's equations in phasor notation we derive (Appendix B)

$$(B\text{-}21) \quad \hat{\rho}_\uparrow = \frac{\hat{B}_\uparrow}{\hat{A}_\uparrow} = - \frac{(\frac{\eta}{R} \cos\theta - 1) + j\cot(\frac{2\pi}{\lambda} d \cos\upsilon)}{(\frac{\eta}{R} \cos\theta + 1) + j\cot(\frac{2\pi}{\lambda} d \cos\theta)}$$

for parallel polarization ($\uparrow$) and

$$(B\text{-}34) \quad \hat{\rho}_\rightarrow = \frac{(\frac{\eta}{R} \sec\theta - 1) - j\cot(\frac{2\pi}{\lambda} d \cos\theta)}{(\frac{\eta}{R} \sec\theta + 1) - j\cot(\frac{2\pi}{\lambda} d \cos\theta)}$$

for perpendicular polarization ($\rightarrow$).

Equations (B-21) and (B-34) were derived to provide confirmation of and limitations on the corresponding expressions in Jasik[5] and to provide a measure of scatter when deviations from design conditions occur. This effort produced an unexpected but welcome result: if the various real and imaginary parts of the numerators in these equations are set equal to zero, it becomes apparent that conditions

for total absorption are possible for off-normal angles of incidence ($\theta \neq 0^{\circ}$). This result allows modification of the Reference "Billboard" Design.

Rectenna Panel Attitude

Setting the numerators of Equations (B-21) and (B-34) equal to zero describes the physical conditions for zero reflection (= 100% absorption) by the Rectenna. Solving these expressions for the conditions of current-sheet-to-reflector separation (d) and current-sheet resistivity (R_o) for any given angle (θ) and wavelength (λ) (Appendix B) yields

$$(B-41) \quad d = (2n - 1) \frac{\lambda}{4} \sec \theta \qquad n = 1,2,3\ldots$$

and either

$$(B-42) \quad R_o = \eta \cos \theta \quad \text{for parallel polarization}$$

or

$$(B-43) \quad R_o = \eta \sec \theta \quad \text{for perpendicular polarization.}$$

Therefore, since the values corresponding to R_o and d can be altered in the actual Rectenna, there appears to be no reason the "billboard" Reference Design Rectenna (Figure 1) cannot be modified to a "flat" configuration (Figure 3). In addition, we believe (without full analysis for confirmation) that this "flat" configuration can be made "terrain-conforming"

by letting R_0 and d vary along the terrain surface. Even

FIGURE 3

"FLAT" RECTENNA CONFIGURATION
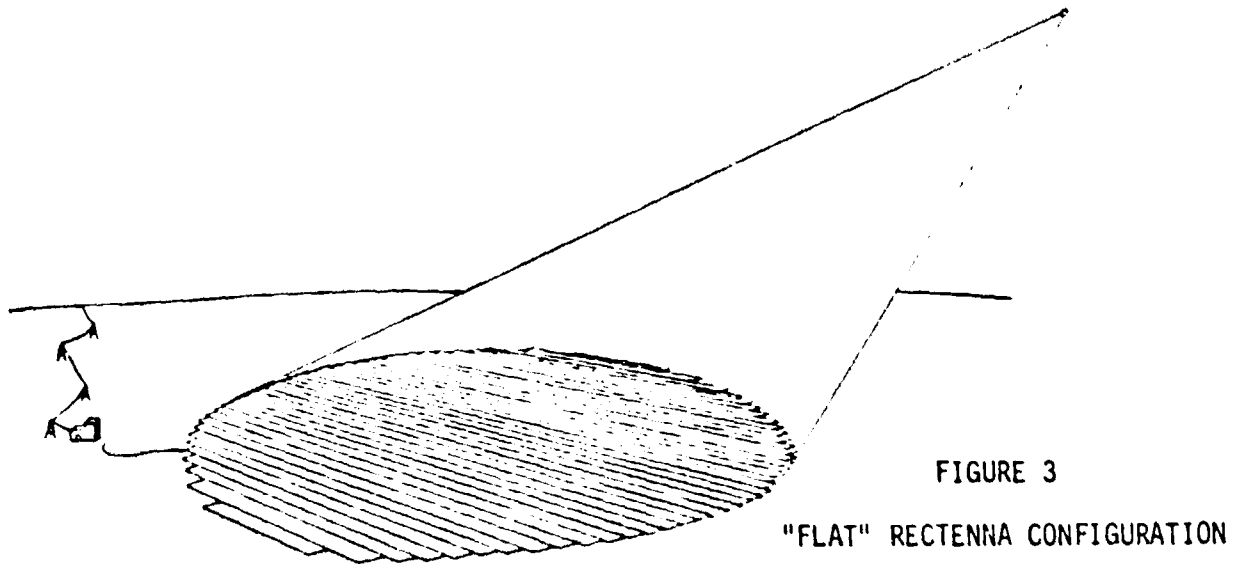
without this last extension, we believe that because of its

ability to eliminate the edge-effect scatter inherent in

the "billboard" sections (Figure 4), and also because it

provides more uniform ground clearance, the "flat" config-

uration deserves serious consideration.
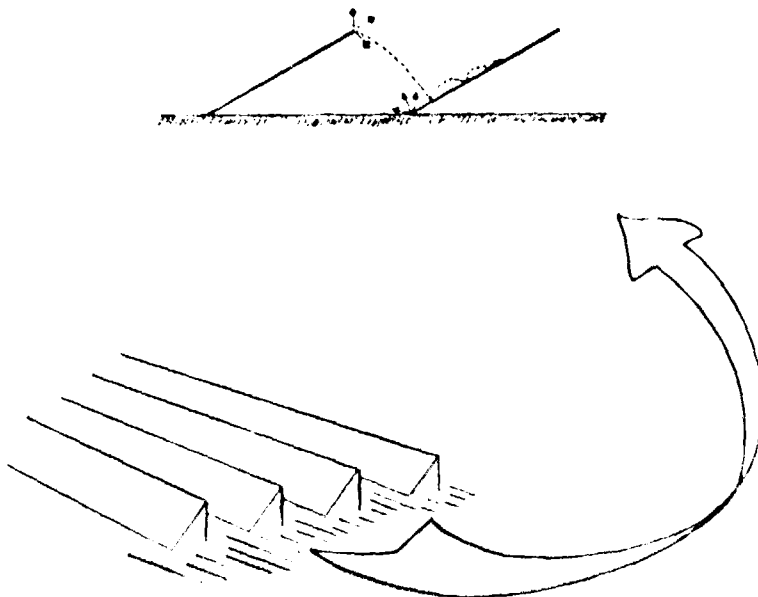
FIGURE 4

"VENETIAN BLIND" SCATTERING SOURCES

An additional advantage of the "terrain conforming"
design lies in the mitigation of certain sources of scatter.
Specular reflection from the "flat" Rectenna would be retro-
reflective only at the equator. For mildly rolling terrain
specular reflections would be scattered as depicted in
Figure 5. But even for the "billboard" configuration,
a slight off-axis orientation can be achieved with minimal
difficulty and with at least some of this advantage.
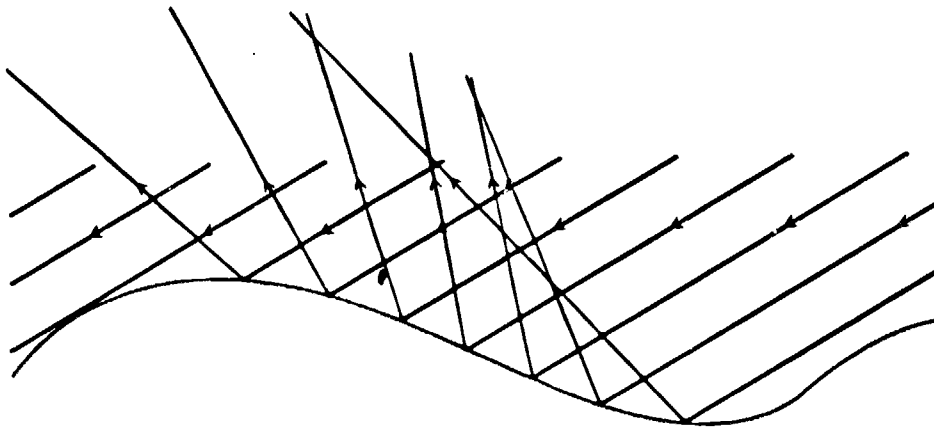
FIGURE 5

RANDOM BACKSCATTER, "TERRAIN CONFORMING" CONFIGURATION

Systematic Deviations

Three c.asses of deviations acting on the rectenna
as a whole ̩an cause the SPS Rectenna to produce
scatter: deviations from design values for

1. impedance,

2. diode-to-reflector spacing, and

3. angle of incidence.

-12-

Such deviations are deducible from Equations (B-21) and (B-34) for whatever design criteria are imposed based upon Equations (B-41) and either (B-42) or (B-43) (see Appendix B).

For the specific case of normal incidence (as in the Reference Design Rectenna), the results of such deviations are given by Equations (E-4), (E-6), and (E-9) (see Appendix E):

$$(E\text{-}4) \qquad |\rho_\uparrow|^2 = |\rho_\rightarrow|^2 \doteq \left[\frac{\eta - R_o}{\eta}\right]^2$$

$$(E\text{-}6) \qquad |\rho_\uparrow|^2 = |\rho_\rightarrow|^2 \doteq \frac{\cot^2 (\frac{2\pi}{\lambda} d)}{4}$$

$$(E\text{-}9) \qquad |\rho_\uparrow|^2 \doteq |\rho_\rightarrow|^2 \doteq \frac{\frac{\theta^4}{4} + \cot^2 (\frac{\pi}{2} \cos \theta)}{4 + \cot^2 (\frac{\pi}{2} \cos \theta)}$$

These equations are represented graphically in Figure 6. For the flat, "terrain-conforming" Rectenna (see pages 11-12), deviations based on conditions given in Equations (B-41) and either (B-42) or (B-43) would produce similar curves. Particularly interesting is the variation of specular reflection due to incidence angle, indicating a measure of importance to station-keeping requirements for the satellite. Because of the dependence of Rectenna circuit impedance on signal strength (see page 30), beam pointing errors translate into mismatch errors.

$|\rho|^2$

0.002

0.001

MW

10

5

0

Reflected Power
@ 5 GW Incident

-10   -5   0   5   10   x

Impedance Mismatch (Ω/Ω)

$\dfrac{Ro-377}{377}$

(a)

$|\rho|^2$

0.01

0.005

MW

50

25

0

Reflected Power
@ 5 GW Incident

.22 .23 .24 .25 .26 .27 .28   d/λ

Current Sheet (Dipole)/Reflector
Seperation

(b)

$|\rho|^2$

0.0002

0.0001

MW

1

0.5

0

Reflected Power
@ 5 GW Incident

-10°   -5°   0°   5°   10°   θ

Angle of Incidence From
Normal
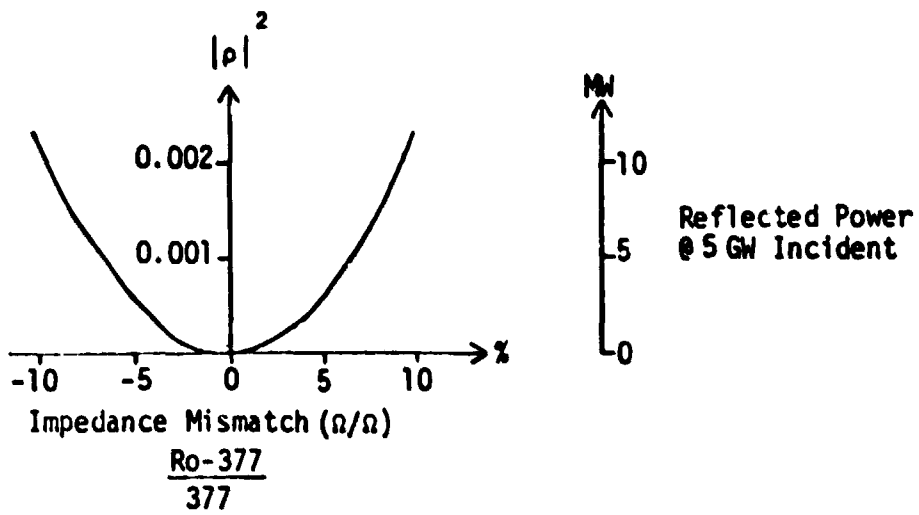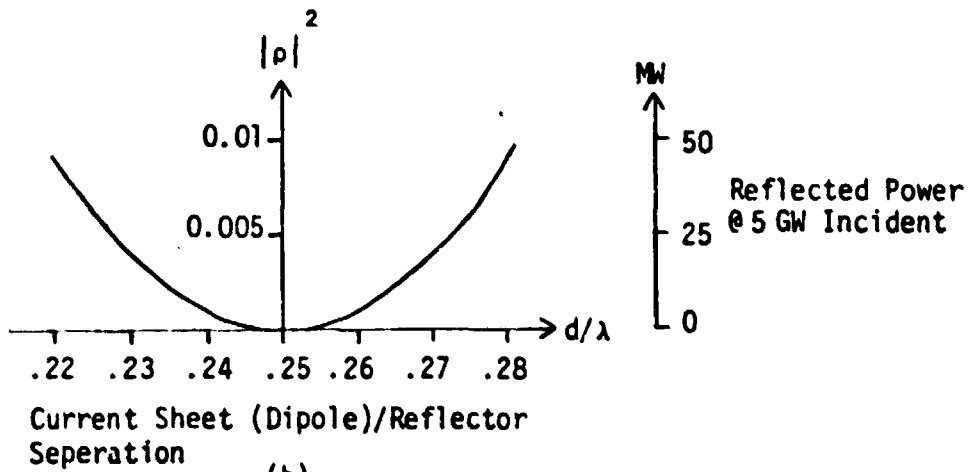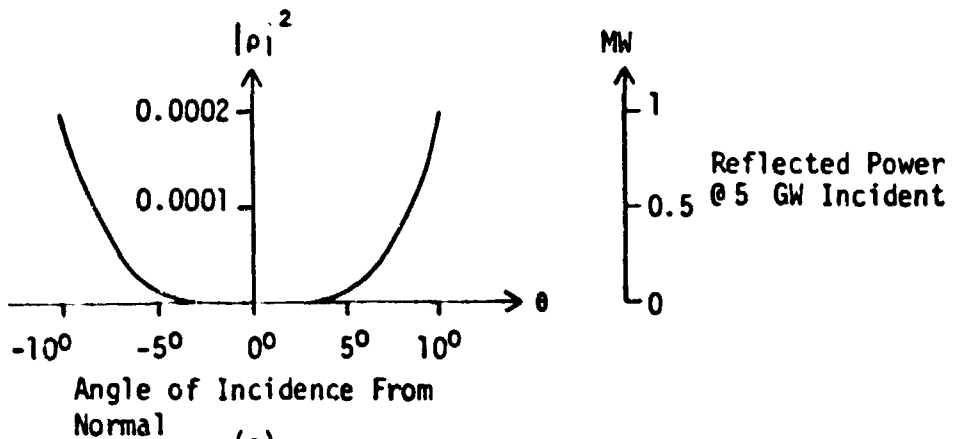
(c)

FIGURE 6

SPECULAR POWER REFLECTION COEFFICIENT AND REFLECTED POWER
LEVEL AS A FUNCTION OF VARIOUS PARAMETERS

-14-

WAVEGUIDE MODEL (WGM)

The CSM provides several insights into the functioning
of the Rectenna and even suggests some potentially useful
modifications, but it does not define limits of element
separation nor does it characterize the Rectenna "near
field." The Waveguide Model, based on the properties of
a special waveguide described by Wheeler[9], permits
quantification of the electromagnetic modes (field configur-
ations) in the immediate vicinity of any Rectenna element.
It must be emphasized, however, that this model can be
applied only to normal incidence.

This waveguide has special imaging characteristics due
to its special construction. Unlike conventional wave-
guides, two opposite walls of this rectangle are magnetic
and non-conductive ($\mu = \infty$, $\sigma = 0$); the other two walls are
perfectly conductive ($\sigma = \infty$)(see Appendix C).

Equations (C-10) and (C-12) suggest the usefulness
of the "mixed-wall" waveguide concept. A probe (monopole
antenna) inserted through one of the conductive walls
will produce images such as those depicted in Figure 7.
The array of images is infinite, and the single monopole
is equivalent to an infinite array of perfectly-spaced
dipoles identically excited. Or, as in Figure 8, an
infinite array of identically-excited dipoles could have
infinitely thin walls forming mixed-wall waveguides erected

between them without altering the field pattern.
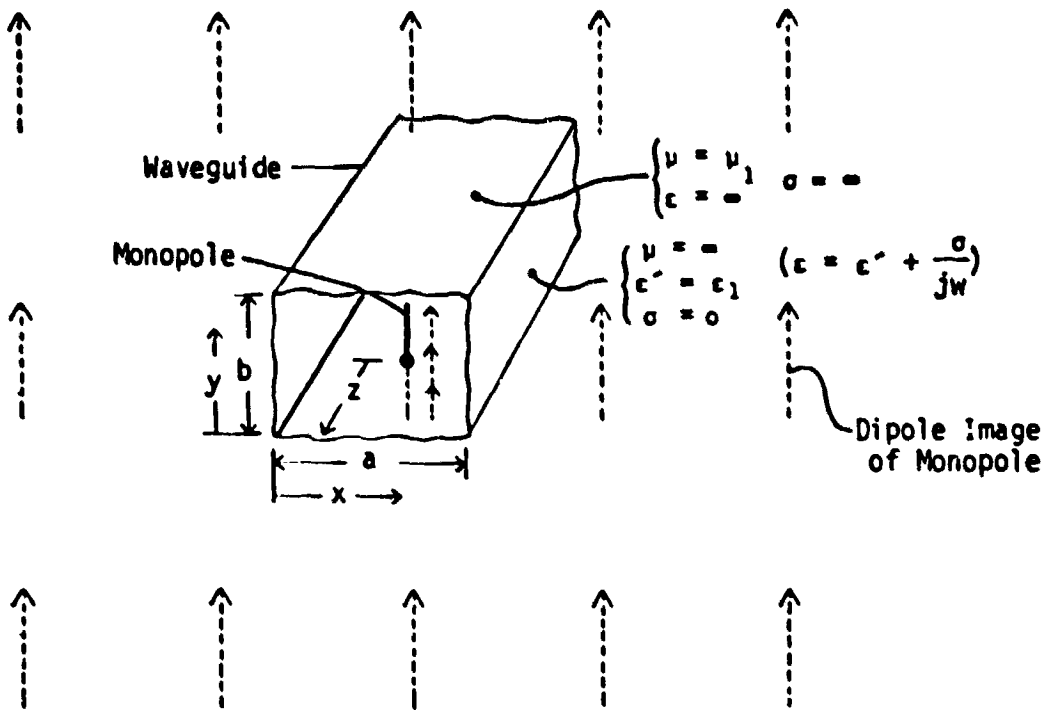
FIGURE 7

IMAGING IN MIXED-WALL WAVEGUIDE
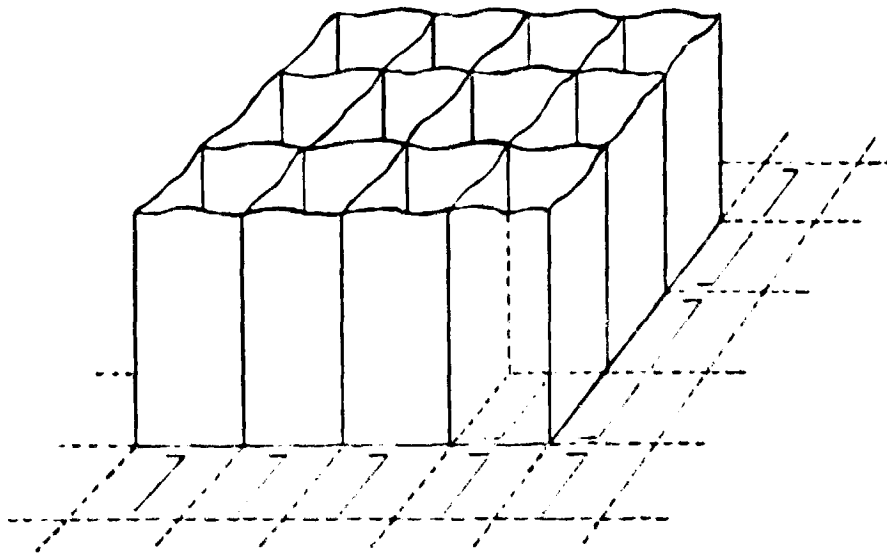
FIGURE 8

MIXED-WALL WAVEGUIDE: PERSPECTIVE

The Imaging Cube

The "Imaging Cube" pictured in **Figures 9-14** provide
a visual representation of the concept of imaging in the
special waveguide model. The cube is constructed of
semi-reflective plastic with a linear light source inside.
Figure 10 is a top view with the light on. In the oblique
views, Figures 11-14, reflections from the walls give the
appearance of an "infinite" array of light bulbs--all reflec-
tions from the single source. This illustrates the manner
in which the WGM generates an infinite array of dipoles.
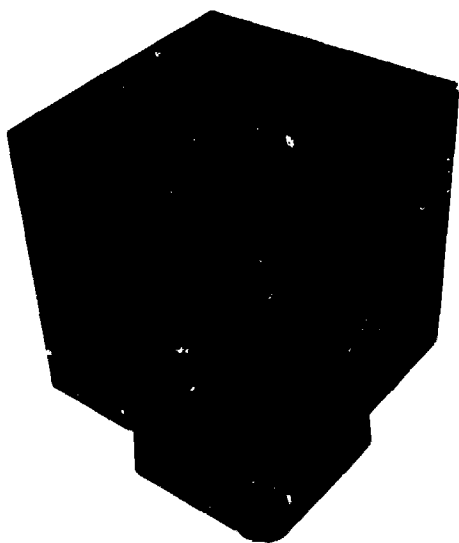
FIGURE 9

NOVAR'S "IMAGING CUBE": PERSPECTIVE
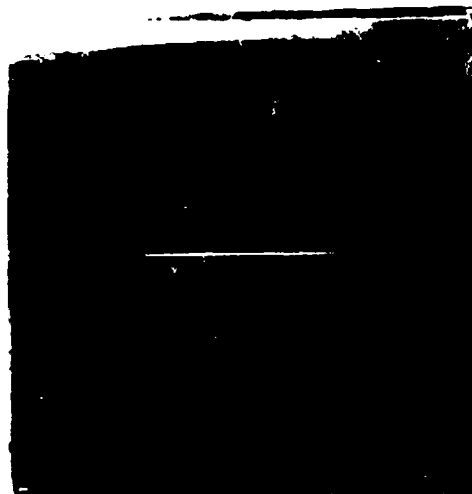
FIGURE 10

"IMAGING CUBE": TOP VIEW

FIGURE 11

FIGURE 12

FIGURE 13
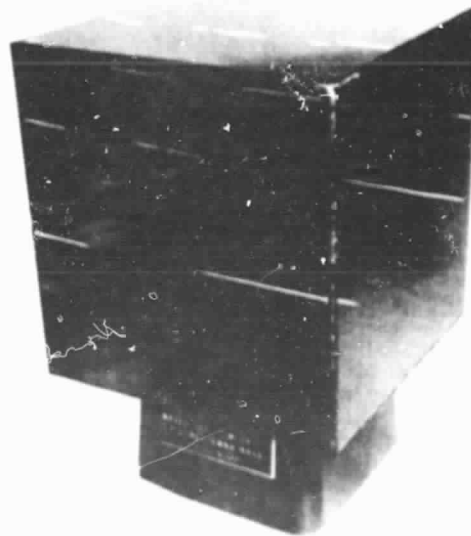
FIGURE 14

FIGURES 11-14 "IMAGING CUBE": REFLECTIONS

Application of Waveguide Model

The WGM allows us to examine the field patterns within any one of the waveguides with the assurance that we know the patterns everywhere above the equivalent infinite array of dipoles. Like the CSM, however, the WGM is restricted to the closeness of the approximation of the infinite array to an actual, very large but finite array.

Analysis of the model of this special waveguide (for derivations, see Appendix C) leads to the conclusion that it is capable of supporting Transverse Electromagnetic modes (TEM's). This suggests that the WGM can be used to represent the infinite array of dipoles, since the TEM's correspond exactly to the plane-wave generated by the array of dipoles. It follows, therefore, that spacings of dipoles (dimensions of the waveguide) exist for which none of the other modes will propagate. These other modes will be present only reactively and will constitute the necessary near-field components which make up the apparent discrepancy between the discrete dipoles of the actual array and the continuous current sheet of the CSM.

Results of the WGM derivations may be consolidated graphically as in Figure 15, in which values of the dimensions "a" and "b" (as defined in Figures 7 and 8) within the hashmarked region would cause all except the TEM and TE_{10} modes to be evanescent. Examination of the field-configuration of the TE_{10} mode indicates that

while this mode is "propagatable" it is not "generatable"
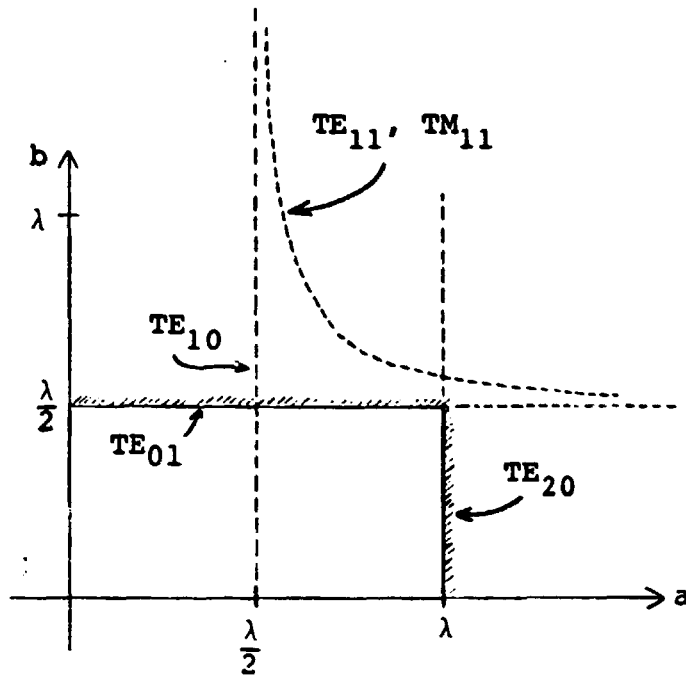
FIGURE 15

LIMITS ON MODES IN MIXED-WALL WAVEGUIDE

at $x = \frac{a}{2}$ since that is a null point for the electric field. Since the model is valid only for ideally distributed and identically excited dipoles, the probe (by definition) can be at no other than the $x = \frac{a}{2}$ position.

The higher order modes in a waveguide (i.e., the non-TEM modes) can be thought of as composed of plane waves reflecting off the side walls and thus propagating along the guide in the axial direction. For two or more identical guides with infinitessimal walls, the distinction between waves reflecting or crossing the walls becomes trivial. Thus we can relate the higher order modes to grating lobes (see below and Appendix D). As the dipoles in the array being modelled move toward one another, the waveguide size shrinks and modes become progressively evanescent, corresponding to grating lobes ceasing to exist. The field components continue to be present, reactively, as "near field."

Since the waveguide dimensions which restrict propagation to the TEM mode are less than λ in the "a" direction and less than $\frac{\lambda}{2}$ in the "b" direction, and since the separation between the centers of the dipoles is a x 2b (Figure 16),
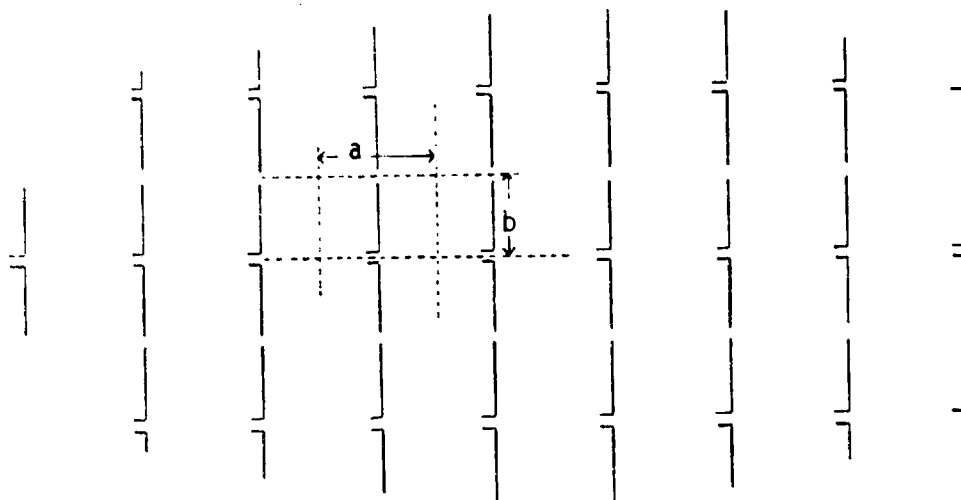
FIGURE 16

WAVEGUIDE MODEL DIMENSIONS

a dipole separation of less than one wavelength in a rect-
angular array will assure no propagating components in grating
lobe directions.

The analyses of both the CSM and the grating lobe
structure predict that a Rectenna can be designed to preclude
specular scattering. By including a reflector the WGM can
also be extended to provide information on this phenomenon.
If a reflector or shorting plate is inserted into the waveguide
behind the monopole (Figure 17) the effect is equivalent to
the infinite array of dipoles depicted in Figure 16 being backed
by a reflector. It is generally accepted that in a conventional
waveguide a properly terminated probe backed by a shorting
plate can, ideally, absorb all power flowing down the waveguide[10].
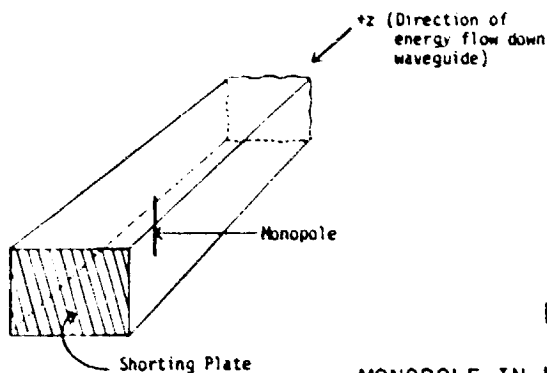
FIGURE 17

MONOPOLE IN MIXED-WALL WAVEGUIDE BACKED
BY SHORTING PLATE

Hence, no specular (vertical) reflection. We believe this
conclusion holds as well for the special waveguide described
here; however a complete proof would require computer analysis
of mode matching (see Appendix C). This analysis is beyond
the scope of the present effort.

Parasitic Reflecting Dipoles

In a conventional waveguide total energy absorption occurs when the shorting plate is placed about $\frac{\lambda}{4}$ behind the monopole. This same condition can be expected to hold for the mixed-wall waveguide. Furthermore, since the shorting plate in an ordinary waveguide can be replaced by an appropriate parasitic element, it is reasonable to expect the same to be possible in the Rectenna (Figure 18). Again, a complete proof of this inference would require generation of the computer analysis suggested above (page 22).

FIGURE 18

RECTENNA WITH PARASITIC REFLECTING
DIPOLE ELEMENTS
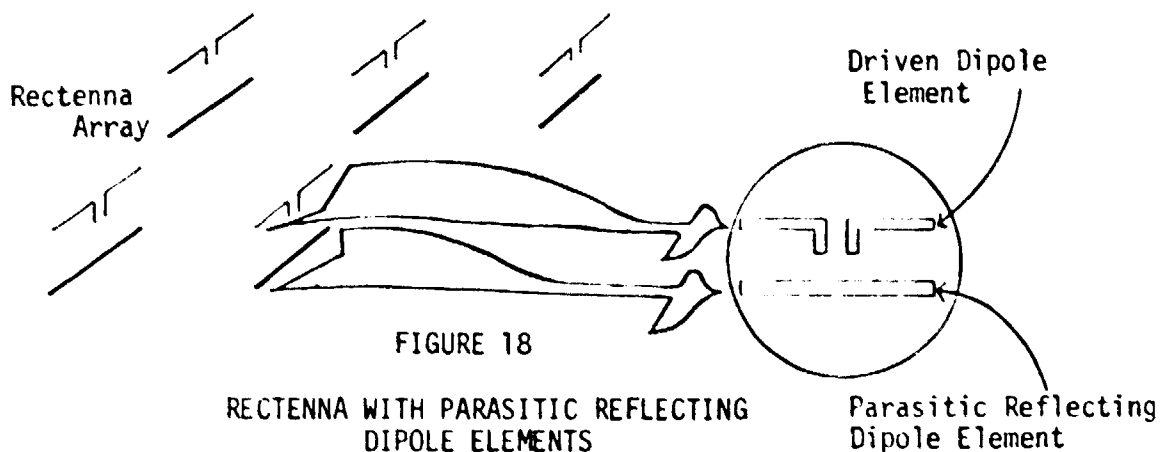
Radiation Resistance

The approximate value of radiation resistance for a dipole located $\frac{\lambda}{4}$ from a perfectly reflecting (shorting) plate in a mixed-wall waveguide, hence in a planar array $\frac{\lambda}{4}$ from a ground plane, is given by Wheeler[9]:

$$R = 377\frac{h^2}{A} \text{ ohms}$$

where

h = effective length of dipole,

A = cross-sectional area of guide.

For a half-wave dipole in the waveguide shown in Figure 19,

$$R = 377 \frac{(\frac{2}{\pi} \frac{\lambda}{2})^2}{(a)(2b)} \qquad \begin{array}{l} a < \lambda \\ 2b < \lambda \end{array}$$

End View   FIGURE 19   Side View
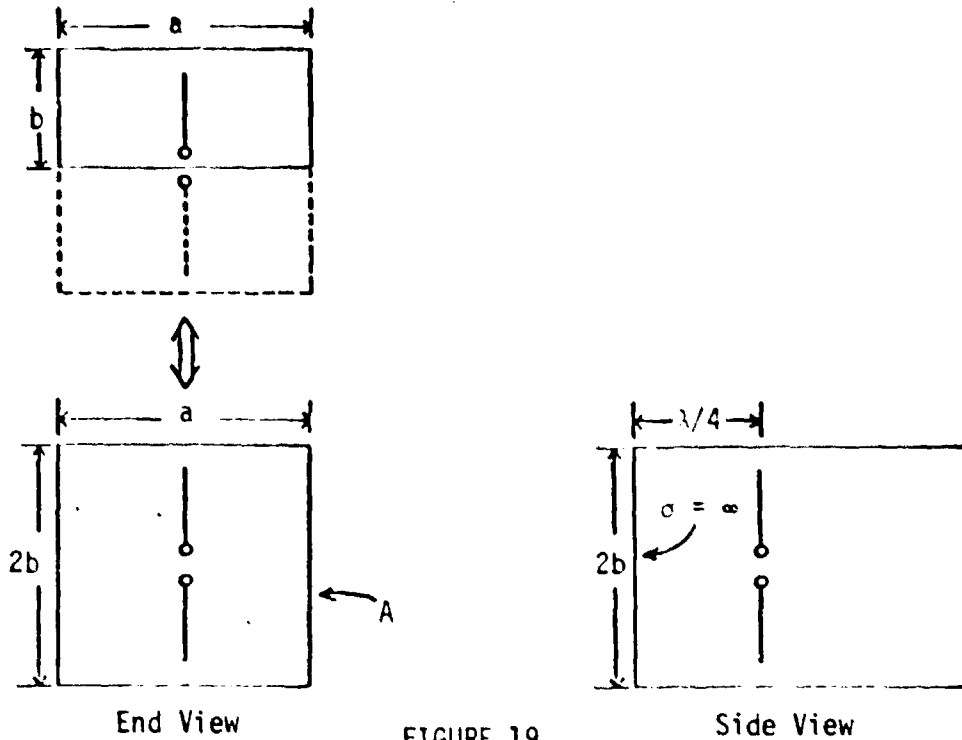
WAVEGUIDE-DIPOLE DEVELOPMENT FOR
RADIATION RESISTANCE

For two cases of some interest,

$$\left. \begin{array}{l} a = 0.5\lambda \\ b = 0.25\lambda \end{array} \right\} \quad R \doteq 152.8\Omega$$

and

$$\left. \begin{array}{l} a = \lambda^- \\ b = 0.5\lambda^- \end{array} \right\} \quad R \doteq 38.2^+\Omega$$

While these expressions and numerical results are clearly

approximate, they do provide a useful idea of the ranges

of resistance values to be expected.

GRATING LOBES

A very satisfactory alternative for element spacing analysis uses the concept of grating lobes. These lobes can be associated with the higher order modes in the waveguide model; evanescence of these modes corresponds to non-existence of the grating lobes (compare Amitay, et al.[4]). For normal incidence grating lobe analysis (See Appendix D) is merely a redundant confirmation of the spacing results of the waveguide model analysis. However, the WGM is not applicable off-normal whereas the grating lobe technique is.

Although specular scattering is not a grating lobe, the presence of specular scattering from an array is established from the same mathematics (See Appendix D).

Specular scattering of the power beam, depicted in Figure 20, is expected to result from most deviations in the Rectenna's parameters. The smaller the deviation anomaly,
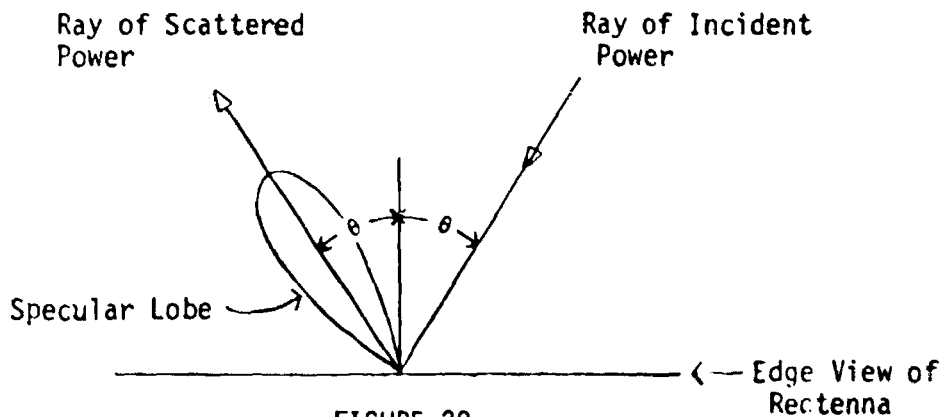
FIGURE 20

DEPICTION OF SPECULAR SCATTERING
FROM FACE OF RECTENNA

the broader will be the specular lobe. Single, isolated element failures (short or open diodes) will appear to radiate as isotropic sources above a reflector.

REPAIRING RECTENNA ELEMENTS

A question has been raised[11] about the problem of locating and servicing faulty Rectenna elements. In light of the foregoing discussion, any failure in a Rectenna element would produce non-directional scattering readily detectable by a directional receiver tuned to the fundamental power-beam frequency. Such a receiver carried aboard a blimp or helicopter operating outside the power-beam path could rapidly and precisely locate a faulty element and relay its location to ground service personnel.

This detection/location system will function adequately with the "billboard" configuration, but even more effectively with the terrain-conforming design because the primary scatter directions leave the best surveillance perspectives clear of the incoming power beam.

The Rectenna dipole-filter-diode assembly and power bus are expected to be the most significant sources of harmonic scattering. The harmonic energy will be concentrated

in grating lobes, as shown in Figure 21.   Random Rectenna
imperfections will broaden the lobes.
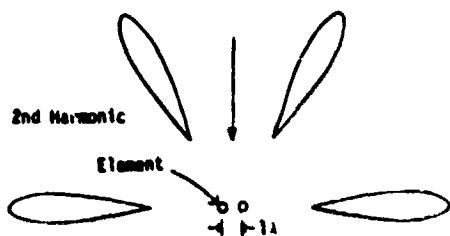
FIGURE 21a

EXAMPLE OF ELEVATION OF
HARMONIC RADIATION
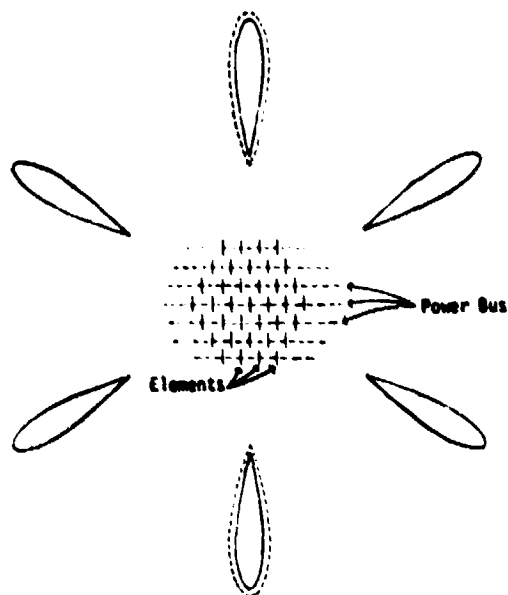
FIGURE 21b

AZIMUTHS OF HARMONIC RADIATION
"Dotted" lobe due to power bus.

FIGURE 21

GRATING LOBE NATURE OF HARMONIC SCATTERING
FROM A RECTENNA

Figures 20 and 21 depict grating lobe directions as the
"tear drop" shape typically anticipated in antenna patterns.
As developed in Appendix D, the pattern for an infinite
array has zero beam width.   The actual rectenna is finite;
nevertheless, we anticipate much narrower beam widths than
those shown for the sake of illustration.

ELEMENT DENSITY

The existence of non-evanescent higher order (TE and TM)
modes corresponds to the existence of grating lobes.   Analysis
of the generation of grating lobes indicates that maximum

center-to-center separation allowable in a _triangular_
Rectenna grid is just under 1.15λ. Since the analysis is
based upon idealizations, we know that this limit is not
attainable in practice. Among the variations from the
ideal are finiteness of the array, finite size of elements,
finite losses in the elements, and apparent changes in the
dielectric constant known to occur in the presence of large
arrays. Since none of these can be fully eliminated, some
deviation is unavoidable. There is insufficient information
at this time for a meaningful evaluation of these deviations.
However, since separation in the Reference Design Rectenna
is approximately 0.6λ, we do believe that the number of
Rectenna elements necessary for total normal plane-wave
absorption can be significantly reduced--better than 2:1.

DEVIATIONS: CAUSES AND AMPLITUDES

Both the CSM and the WGM analyses confirm total absorp-
tion (zero scatter) for the ideal beam of incident energy
impinging under ideal conditions upon ideal Rectenna elements.
Such conditions can be approximated in practice.

We have shown in the CSM analysis that for a uniform
incident plane-wave signal, when the conditions of Equations
(B-41) and either (B-42) or (B-43) are met, the reflected
component is eliminated (page 10). When the incident signal
is not uniform it can be understood to be composed of both
a uniform component and a non-uniform or deviant component.

Analysis of these components by superposition is discussed in Appendix E along with an approach to evaluating the effect of the deviant component. Further analysis must wait until more information is available to describe the expected deviant component.

In reality, the Rectenna dipole-diode response to non-uniform incident radiation is not perfectly linear. Assuming that a dipole "sees" an effective impedance reflected through the first filter (Figure 22), this impedance depends upon the strength of the signal impinging upon that diode.
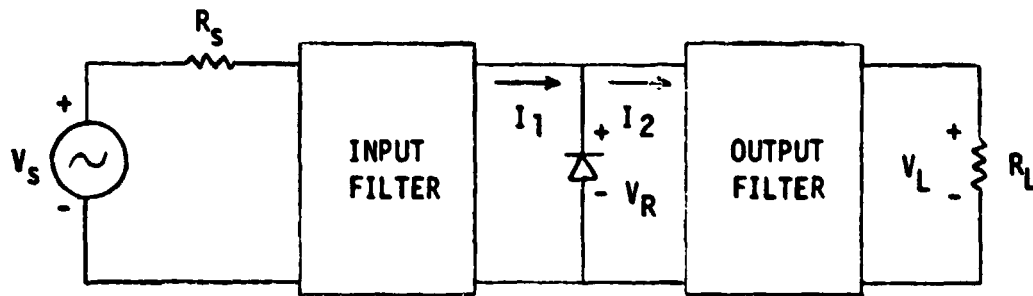
FIGURE 22

SIMPLIFIED RECTENNA ELEMENT CIRCUIT
(After Gutmann and Borrego)

The Gutmann-Borrego[12,13] model is quite adequate for a Reference Design Rectenna as seen by the bus. Filters of the sort shown can be expected to provide isolation at undesired harmonics while providing coupling at desired frequencies. Thus the fundamental voltage produced on the dipole is impressed on the diode.

Although harmonic as well as fundamental and zero-frequency currents exist at the diode, to the extent that the filters are ideal only fundamental currents can exist at the dipole. Thus the dipole "sees" a true impedance; this implies that this linear load will vary with signal level--an apparent contradiction. This follows from the fact that the amplitude of the fundamental current at the diode is not linearly related to the amplitude of the fundamental voltage. The situation appears to be further complicated by the presence of the bus which provides, through the output filter, a zero-frequency operating point dependent upon the weighted average of the signal strengths at all Rectenna dipoles, and perhaps also on the electrical properties of the equipment carrying Rectenna energy to the power grid.

If these difficulties have been resolved we are not aware of it; if not, we recommend careful analysis and/or experimentation.

It is worth noting that this non-linearity does not appear intuitively to be a problem for ideal conditions, since the diode is loaded by an impedance whose value can be determined and adjusted experimentally and/or analytically.

EXTERNAL DISTURBANCES

Several mechanisms can affect signal qualities at a particular location on the Rectenna grid. The most significant

of these are ionospheric and lower atmospheric (combined here as "atmospheric") phenomena and "aircraft" overflights.

Atmospheric phenomena cause polarization shifts and amplitude fluctuations in an EM wave at microwave frequencies.[14,15,16,17,18,19,20,21] However, only infrequent depolarizing events no greater than 20 dB (1% scattered power) have so far been observed in downlink transmissions through apertures larger than 10 m^2. These observations suggest that depolarization should not be a significant source of scatter.

Amplitude fluctuations cause scatter by disrupting uniform illumination. Further, this deviation from design RF power values causes impedance mismatches at the diodes, resulting in further scattering.

Previous satellite to earth propagation measurements are only marginally applicable to the Satellite Power System because of aperture averaging effects. The minimum aperture for previous studies has been on the order of $5000\lambda^2$. On the other hand, the aperture for each "independent" element of the Rectenna is about $1\lambda^2$. Hence, amplitude fluctuations which would average out for the larger apertures may cause amplitude fluctuations appreciably greater than 0.1 dB for the Rectenna.

Another limitation on the applicability of previous studies is their use of modulated signals. Most deep fades are frequency sensitive. Thus, for modulated signals

taken on the C and S bands with power spread over a spectrum of frequencies, the observed amplitude fluctuations can be expected to be less than those in a monochromatic SPS power beam.

Another potential source of signal disturbance is overflights of the Rectenna by relatively large objects-- aircraft. Such an object would momentarily interrupt the power beam to a portion of the Rectenna, causing diffraction patterns (Figure 23). Preliminary evidence obtained by

Possible 6-9dB
Signal Increase
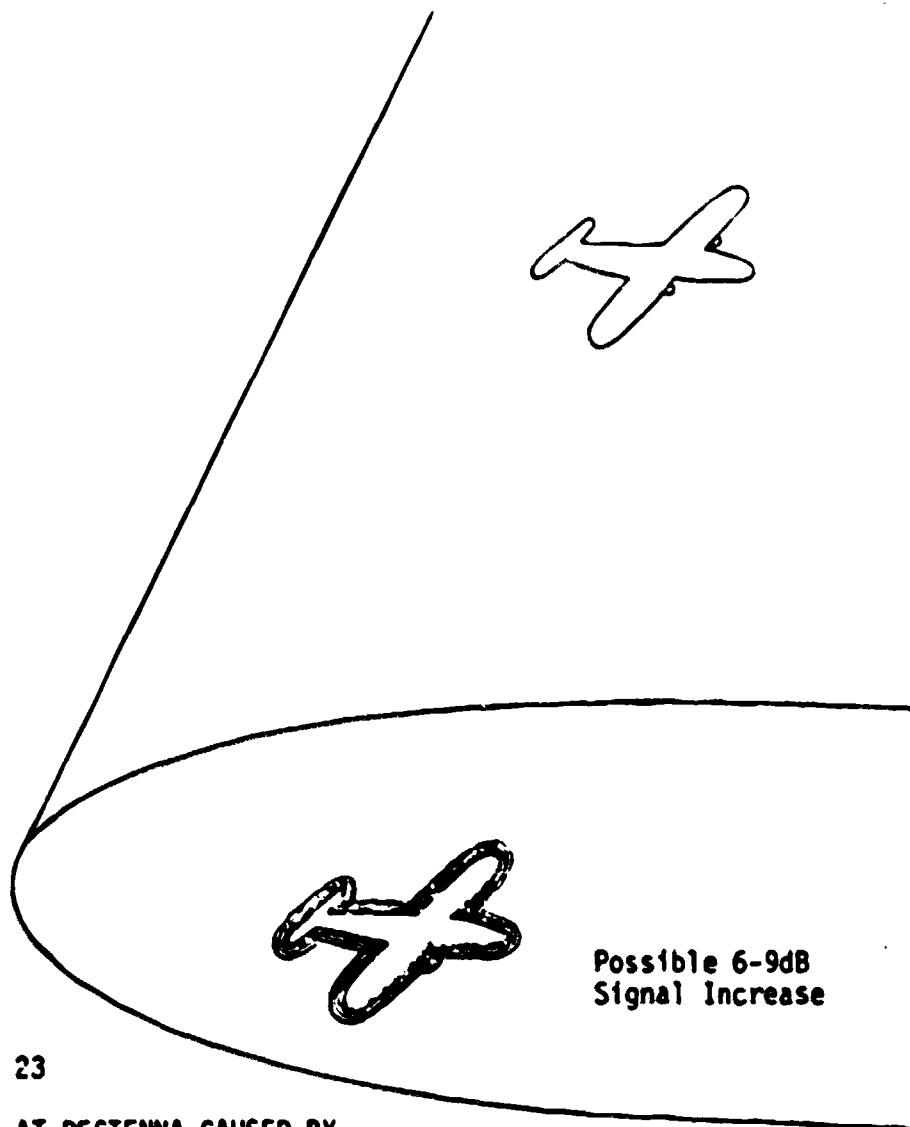
FIGURE 23

DIFFRACTION ENHANCEMENT AT RECTENNA CAUSED BY
OBJECT FLYING THROUGH THE POWER BEAM

experiment indicates that, depending upon the relative
size and shape of the object, large signal increases may be
generated. An actual overflight of the Novar earth station
by a light aircraft produced the signal trace shown in
Figure 24. Although the circumstances of both tests leave
room for question concerning signal-variation amplitudes,
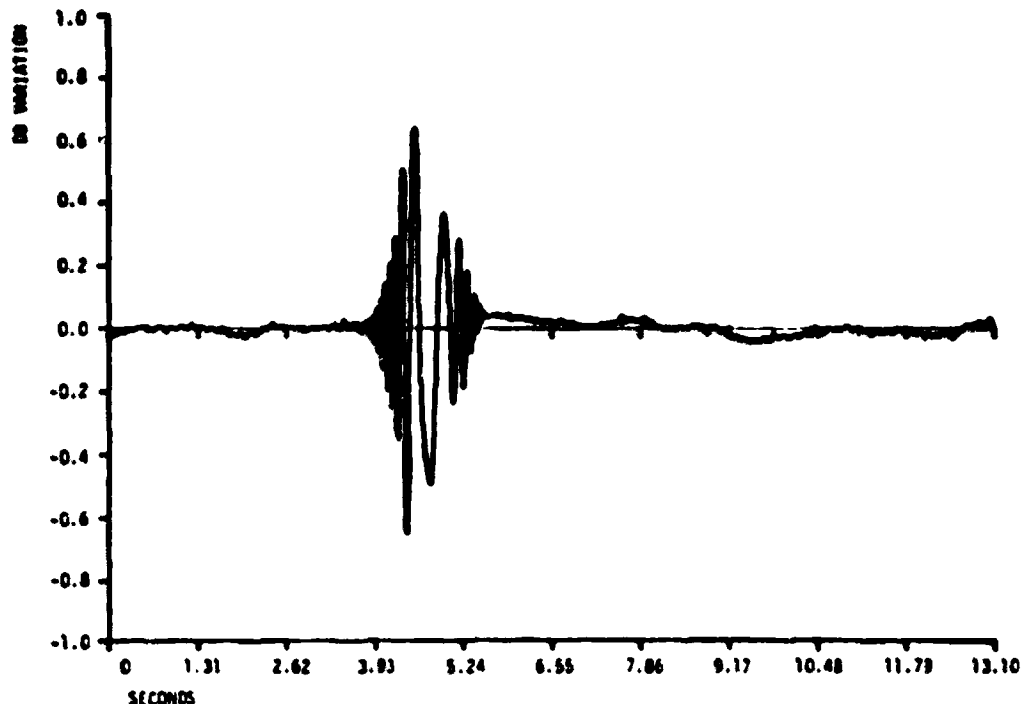
FIGURE 24

SIGNAL DEVIATION CAUSED BY OVERFLIGHT

they do make it quite clear that there is a potential problem
and that Rectenna diodes should be manufactured with sufficient
surge-tolerance to accept transient voltage overloads of this
magnitude and with sufficient heat-tolerance to protect
them against overheating due to the passage of slower objects.

The field distribution pattern can be examined in connection with atmospheric patterns by a method comparable to that of Appendix E to determine scatter patterns and amplitudes if there is concern that undesireably high signals might be scattered.

ACKNOWLEDGEMENTS

REFERENCES

1. W. C. Brown, "The Technology and Application of Free-Space Power Transmission by Microwave Beam," Proc. IEEE, Vol. 62, No. 1, pp. 11-25, Jan. 1974.

2. W. C. Brown, "Optimization of the Efficiency and Other Properties of the Rectenna Element," 1976 IEEE MTT-S International Microwave Symposium: Digest of Technical Papers, pp. 142-144.

3. R. M. Dickinson, "Performance of a High-Power 2.388-GHz Receiving Array in Wireless Power Transmission Over 1.54 km," 1976 IEEE MTT-S International Microwave Symposium: Digest of Technical Papers, pp. 139-141.

4. N. Amitay, V. Galindo, and C. P. Wu, Theory and Analysis of Phased Array Antennas. New York: Wiley-Interscience, 1972.

5. H. Jasik (ed), Antenna Engineering Handbook. New York: McGraw-Hill, 1961. (The Salisbury screen is described in Sec. 32, p. 36.)

6. J. D. Kraus, Electromagnetics. New York: McGraw-Hill, 1953. ("Space cloth" is discussed, starting on p. 407.)

7. James R. Wait, "On the Theory of Scattering from a Periodically Loaded Wire Grid," IEEE Trans. Antennas and Propagation, Vol. AP19, pp. 409-413, May 1977.

8. James R. Wait, "Reflection at Arbitrary Incidence from a Parallel Wire Grid," Applied Scientific Research, Section B, Vol. 4, 1955.

9. H. A. Wheeler, "The Radiation Resistance of an Antenna in an Infinite Array or Waveguide," Proc. IRE, Vol. 36, No. 4, pp. 478-487, Apr. 1948. (Introduces concept of waveguide to image interchange. Gives radiation resistance of each element of an infinite rectangular array on the basis of a special waveguide. States ability of individual antenna in guide with reflector to have 100% absorption.)

10. J. C. Slater, Microwave Transmission. New York: McGraw-Hill, 1942. (Good basic treatment including a careful discussion of the limitation of "impedance" in waveguides. Discusses dipole-waveguide connection on p. 296.)

11. P. J. Donalek and J. L. Whysong, "Unity Interface Requirements For A Solar Power System," Karza Engineering Company, Chicago, DOE/ER-0032, Sept. 1978.

12. Ronald J. Gutmann and Jose M. Borrego, "Solar Power Satellite Rectenna Design Study: Directional Receiving Element and Parallel-Series Combining Analysis," Rensselaer Polytechnic Institute Report, Dec. 1978.

13. Ronald J. Gutmann and Jose M. Borrego, "Power Combining in Microwave Power Rectifiers," IEEE Trans. Microwave Theory and Tech., Vol. MTT 27, pp. 958-963, Dec. 1979.

14. R. R. Taur, "Ioncspheric Scintillation at Frequencies Above 1 Ghz.," Comsat Technical Review, Vol. 4, No. 2, pp. 462-476, Fall 1974.

15. J. P. Basart, G. K. Miley, and B. G. Clark, "Phase Measurements with an Interferometer Baseline of 11.3 km" IEEE Trans. Antennas and Propagation, Vol. AP18, No. 3, pp. 375-379, May 1970. (Provides good insight into phase variations due to the atmosphere.)

16. D. J. Fang, "Attenuation and Phase Shift of Microwave due to Canted Raindrops," Comsat Technical Review, Vol. 5, No. 1, pp. 135-157, Spring 1975.

17. D. J. Fang and J. Jih, "A Model of Microwave Propagation Along an Earth Satellite Path," Comsat Technical Review, Vol. 6, No. 2, pp. 379-411, Feb. 1976.

18. M. C. Thompson, Jr. and H. B. Janes, "Antenna Aperture Size Effect on Tropospheric Phase Noise," IEEE Trans. Antennas and Propagation, Vol. AP14, pp. 800-802, Nov. 1966.

19. R. K. Crane and D. W. Blood, Handbook for the Estimation of Microwave Propagation Effects--Link Calculations for Earth-Spaced Paths (Path Loss and Noise Estimation), Environmental Research & Technology, Inc., Technical Report No. 1, p. 7376, June 1979.

20. R. R. Taur, "Ionospheric Scintillation at 4 and 6 GHz," Comsat Technical Review, Vol. 3, No. 1, pp. 145-163, Spring 1973.

21. R. K. Crane, "Ionospheric Scintillation," Proc. IEEE, pp. 180-198, Feb. 1977.

D_2

APPENDIX A

PLANE WAVE DERIVATION

PLANE WAVE DERIVATION

The derivations upon which much of this report is based make great use of transmission and reflection of plane waves. The characteristics of plane waves can be derived from Maxwell's equations[*]:

(A-1) $\quad \nabla \times \hat{\underline{E}} = -j\omega\mu\hat{\underline{H}}$

(A-2) $\quad \nabla \times \hat{\underline{H}} = \sigma\hat{\underline{E}} + j\omega\epsilon'\hat{\underline{E}} = j\omega(\epsilon' + \frac{\sigma}{j\omega})\,\hat{\underline{E}}$

$$= j\omega\epsilon\hat{\underline{E}} \qquad (\epsilon = \epsilon' - j\epsilon'' = \epsilon' + \frac{\sigma}{j\omega})$$

(A-3) $\quad \nabla \cdot \hat{\underline{E}} = 0 \qquad\qquad$ (Charge-free region)

(A-4) $\quad \nabla \cdot \hat{\underline{H}} = 0$

from which we can derive wave equations by the usual procedure

$$\nabla \times \nabla \times \hat{\underline{E}} = \nabla \times (-j\omega\mu\hat{\underline{H}})$$

$$\nabla(\nabla \cdot \hat{\underline{E}}) - \nabla^2\hat{\underline{E}} = -j\omega\mu(\nabla \times \hat{\underline{H}})$$

$$- \nabla^2\hat{\underline{E}} = -j\omega\mu(j\omega\epsilon\hat{\underline{E}})$$

(A-5) $\quad \nabla^2\hat{\underline{E}} = -\omega^2\mu\epsilon\hat{\underline{E}} \qquad$ (Wave equation in $\hat{\underline{E}}$)

Similarly

(A-6) $\quad \nabla^2\hat{\underline{H}} = -\omega^2\mu\epsilon\hat{\underline{H}} \qquad$ (Wave equation in $\hat{\underline{H}}$)

For a plane wave moving in the +z' direction

$$\hat{E}_{z'} = \hat{H}_{z'} = 0$$

---

*We will adopt the notation that the underbar (_) implies a vector quantity while the "hat" (^) implies a phasor.
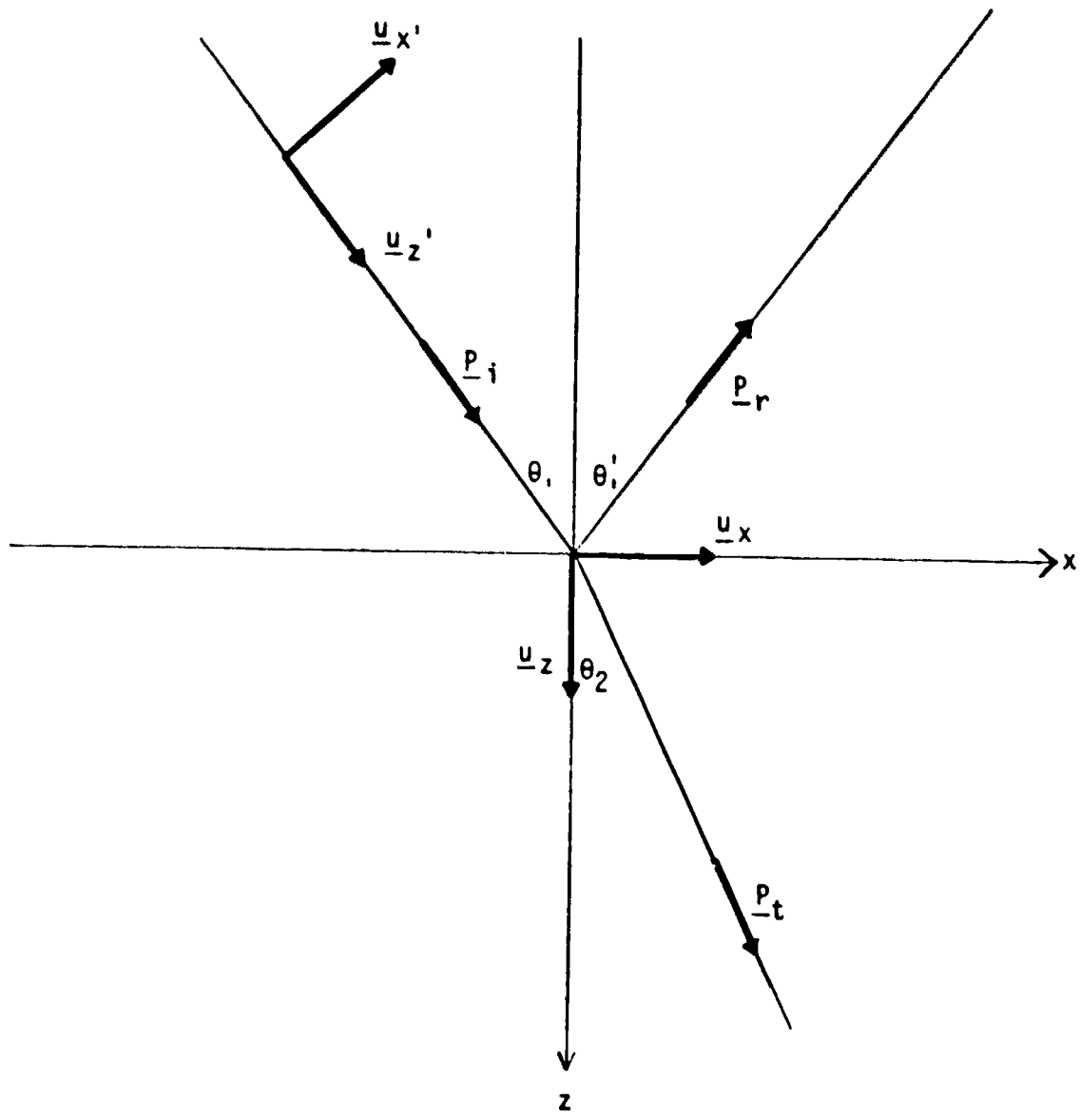
FIGURE A-1

PLANE WAVE REFLECTION GEOMETRY

and

$$\frac{\partial(\,)}{\partial x'} = \frac{\partial(\,)}{\partial y'} = 0$$

Thus, the wave equation in $\hat{\underline{E}}$ becomes

(A-7) $\qquad \nabla^2 \hat{\underline{E}} = \frac{\partial^2}{\partial z'^2} \hat{\underline{E}} = -\omega^2 \mu \epsilon \hat{\underline{E}}$ $\qquad\qquad (\hat{\underline{E}} = \underline{u}_{x'} \hat{E}_{x'} + \underline{u}_{y'} \hat{E}_{y'})$

yielding

(A-8) $\qquad \hat{\underline{E}} = \hat{\underline{A}} e^{-j\omega\sqrt{\mu\epsilon}z'}$

$\qquad\qquad = \hat{\underline{A}} e^{-jkz'}$

where $k \cdot \equiv \cdot \omega\sqrt{\mu\epsilon}$ (The symbol $\cdot \equiv \cdot$ indicates a defining relation.)

(A-8') $\qquad \hat{\underline{E}} = \underline{u}_{x'} \hat{A}_{x'} e^{-jkz'} + \underline{u}_{y'} \hat{A}_{y'} e^{-jkz'}$

From Equation (A-1)

(A-1') $\qquad \hat{\underline{H}} = -\frac{1}{j\omega\mu} \nabla \times \hat{\underline{E}}$

which reduces for our case to

(A-9) $\qquad \hat{\underline{H}} = \frac{1}{j\omega\mu} (\underline{u}_{x'} \frac{\partial}{\partial z'} \hat{E}_{y'} - \underline{u}_{y'} \frac{\partial}{\partial z'} \hat{E}_{x'})$

$\qquad\qquad = \eta^{-1} (-\underline{u}_{x'} \hat{A}_{y'} e^{-jkz'} + \underline{u}_{y'} \hat{A}_{x'} e^{-jkz'})$

where $\eta \cdot \equiv \cdot \sqrt{\frac{\mu}{\epsilon}}$

If we change notation (See Figure A-1) we can write

(A-10) $\qquad \hat{\underline{E}} = \underline{u}_{x'} \hat{A}_{\uparrow} e^{-jkz'} + \underline{u}_{y'} \hat{A}_{\rightarrow} e^{-jkz'}$

(A-11) $\qquad \hat{\underline{H}} = \eta^{-1} (-\underline{u}_{x'} \hat{A}_{\rightarrow} e^{-jkz'} + \underline{u}_{y'} \hat{A}_{\uparrow} e^{-jkz'})$

where subscripts $\uparrow$ and $\rightarrow$ refer to the polarization.

Polarization is defined by the relationship of the incident wave's electric field vector, $\hat{\underline{E}}$, to the plane of incidence. This plane is determined by rays in the directions

-41-

of propagation of the incident and reflected waves (See Figure A-1). When $\hat{\underline{E}}$ is parallel to the plane of incidence, the wave is said to be parallel polarized ($\uparrow$); when perpendicular, perpendicularly polarized ($\rightarrow$). Any other polarization can be decomposed into a combination of parallel and perpendicular polarization. Note that when the z = 0 plane is horizontal the terms "vertical" ($\uparrow$) and "horizontal" ($\rightarrow$) are appropriate to describe the polarization.

For applications involving reflections we wish to describe plane waves in terms of a coordinate system tied to the interface between regions. We will make use of the coordinate shift

$$\underline{u}_{x'} = \underline{u}_x \cos\theta_1 - \underline{u}_z \sin\theta_1 \qquad x' = x \cos\theta_1 - z \sin\theta_1$$

$$\underline{u}_{z'} = \underline{u}_z \sin\theta_1 + \underline{u}_z \cos\theta_1 \qquad z' = x \sin\theta_1 + z \cos\theta_1$$

$$\underline{u}_{y'} = \underline{u}_y \qquad\qquad\qquad y' = y$$

Under this coordinate shift the incident wave is

(A-12) $\hat{\underline{E}}_i = (\underline{u}_x \cos\theta_1 - \underline{u}_z \sin\theta_1) \hat{A}_\uparrow e^{-jk_1(x \sin\theta_1 + z \cos\theta_1)}$

$$+ \underline{u}_y \hat{A}_\rightarrow e^{-jk_1(x \sin\theta_1 + z \cos\theta_1)}$$

(A-13) $\hat{\underline{H}}_i = \eta^{-1} [\underline{u}_y \hat{A}_\uparrow e^{-jk_1(x \sin\theta_1 + z \cos\theta_1)}$

$$+ (-\underline{u}_x \cos\theta_1 + \underline{u}_z \sin\theta_1) \hat{A}_\rightarrow e^{-jk_1(x \sin\theta_1 + z \cos\theta_1)}]$$

Similarly, the reflected wave is

(A-14) $\hat{\underline{E}}_r = (\underline{u}_x \cos\theta_1' + \underline{u}_z \sin\theta_1') \hat{B}_\uparrow e^{-jk_1(x \sin\theta_1' - z \cos\theta_1')}$

$$+ \underline{u}_y \hat{B}_\rightarrow e^{-jk_1(x \sin\theta_1' - z \cos\theta_1')}$$

(A-15) $\hat{\underline{H}}_r = -\eta_1^{-1}\{\underline{u}_y\hat{B}_\uparrow e^{-jk_1(x\sin\theta_1' - z\cos\theta_1')}$

$\qquad - (\underline{u}_x\cos\theta_1' + \underline{u}_z\sin\theta_1')\hat{B}_\rightarrow e^{-jk_1(x\sin\theta_1' - z\cos\theta_1')}\}$

and the transmitted (refracted) wave is

(A-16) $\hat{\underline{E}}_t = (\underline{u}_x\cos\theta_2 - \underline{u}_z\sin\theta_2)\hat{F}_\uparrow e^{-jk_2(x\sin\theta_2 + z\cos\theta_2)}$

$\qquad + \underline{u}_y\hat{F}_\rightarrow e^{-jk_2(x\sin\theta_2 + z\cos\theta_2)}$

(A-17) $\hat{\underline{H}}_t = \eta^{-1}\{\underline{u}_y\hat{F}_\uparrow e^{-jk_2(x\sin\theta_2 + z\cos\theta_2)}$

$\qquad + (-\underline{u}_x\cos\theta_2 + \underline{u}_z\sin\theta_2)\hat{F}_\rightarrow e^{-jk_2(x\sin\theta_2 + z\cos\theta_2)}\}$

$\qquad$ where $k_1 \cdot \equiv \cdot \omega\sqrt{\mu_1\epsilon_1}$

$\qquad\qquad k_2 \cdot \equiv \cdot \omega\sqrt{\mu_2\epsilon_2}$

$\qquad\qquad \eta_1 \cdot \equiv \cdot \sqrt{\dfrac{\mu_1}{\epsilon_1}}$

$\qquad\qquad \eta_2 \cdot \equiv \cdot \sqrt{\dfrac{\mu_1}{\epsilon_1}}$

APPENDIX B

CURRENT SHEET MODEL

CURRENT SHEET MODEL

One very useful model of the Rectenna is based on the
current sheet equivalency of a large planar array above a
reflector as shown in Figure B-1. The current sheet has
many of the properties of resistive absorbers described by
Jasik [5] and Kraus [6]. The model is mathematically characterized
by an expression for the fraction of the incident plane wave
that is reflected from the sheet.

Incident Power

Current Sheet

Infinitely Conductive Reflector
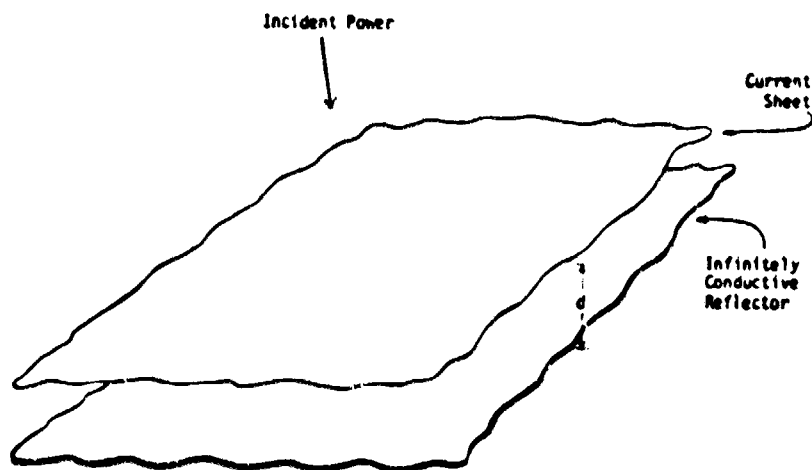
FIGURE B-1

CURRENT SHEET MODEL

Justification for using a current sheet model involving
uniformly distributed currents to model the obviously discrete
dipoles of the reference system Rectenna is based primarily on
work of Wait [7,8]. Conceptually, we can also justify the model

PRECEDING PAGE BLANK NOT FILMED

-47-

for normal incidence by comparing it to the waveguide model
(Appendix C) in which evanescent modes, present as "beyond
cutoff", correspond to the "near-field" components which
become negligible at any significant distance from the antenna
array. For the moment we shall simply claim that element
spacing is small enough and the rectenna is sufficiently
large to justify the model.

Figure B-2 represents a cross-section of the current
sheet (Figure B-1), with Poynting's vectors for incoming and
reflected signals. Total absorption corresponds to cancella-
tion of the reflected component in Region 1 by the partial
transmission upward through the current sheet. A "field
reflection coefficient" for Region 1 can be found by means
of the plane wave derivations from Appendix A. Parallel and
perpendicular polarization are derived separately.
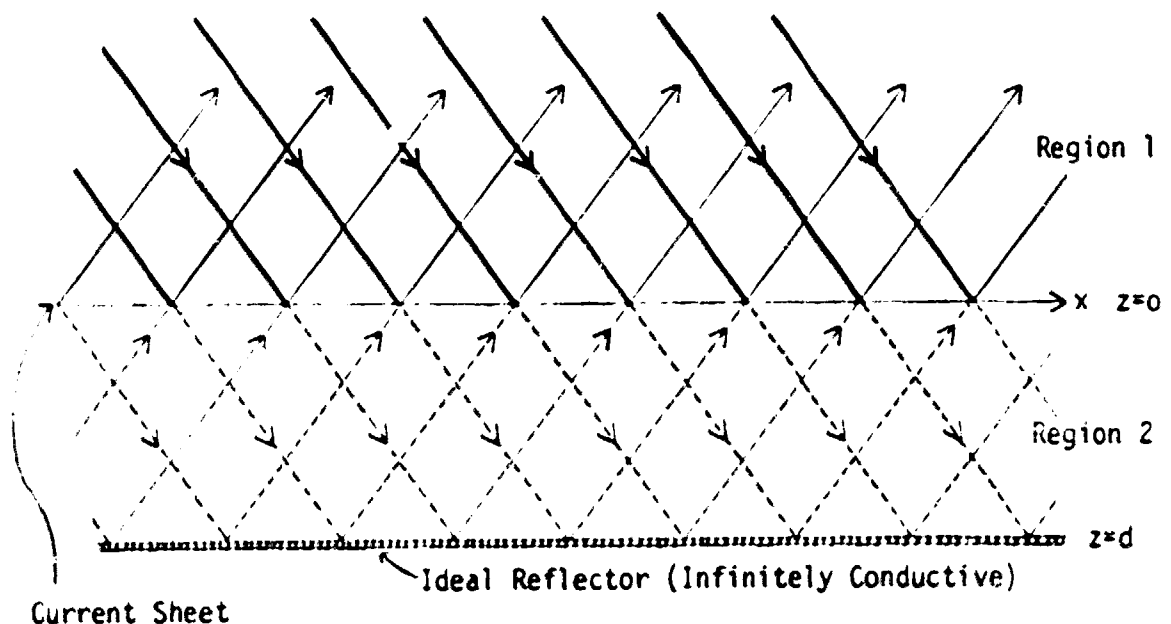
FIGURE B-2

CURRENT SHEET MODEL CROSS-SECTION

PARALLEL POLARIZATION

For Region 1 $(z < 0)$:

(B-1) $\hat{\underline{E}}_1 = (\underline{u}_x \cos\theta - \underline{u}_z \sin\theta)\, \hat{A}_\uparrow e^{-jk(x\sin\theta + z\cos\theta)}$

$+ (\underline{u}_x \cos\theta + \underline{u}_z \sin\theta)\, \hat{B}_\uparrow e^{-jk(x\sin\theta - z\cos\theta)}$

(B-2) $\hat{\underline{H}}_1 = \underline{u}_y\, \eta^{-1}\, [\hat{A}_\uparrow e^{-jk(x\sin\theta + z\cos\theta)} - \hat{B}_\uparrow e^{-jk(x\sin\theta - z\cos\theta)}]$

Similarly, for Region 2 $(0 < z < d)$:[*]

(B-3) $\hat{\underline{E}}_2 = (\underline{u}_x \cos\theta - \underline{u}_z \sin\theta)\, \hat{F}_\uparrow e^{-jk(x\sin\theta + z\cos\theta)}$

$+ (\underline{u}_x \cos\theta + \underline{u}_z \sin\theta)\, \hat{G}_\uparrow e^{-jk(x\sin\theta - z\cos\theta)}$

(B-4) $\hat{\underline{H}}_2 = \underline{u}_y\, \eta^{-1}\, [\hat{F}_\uparrow e^{-jk(x\sin\theta + z\cos\theta)} - \hat{G}_\uparrow e^{-jk(x\sin\theta - z\cos\theta)}]$

Examination of the boundary conditions on the tangential
component $(\hat{E}_{tan} = 0)$ at the infinitely conductive reflector
surface at $z = d$ yields

(B-5) $\underline{u}_x \cos\theta\, (\hat{F}_\uparrow e^{-jkd\cos\theta} + \hat{G}_\uparrow e^{+jkd\cos\theta})\, e^{-jkx\sin\theta} \overset{x,y}{\equiv} 0$

(B-6) $\hat{G}_\uparrow = -\hat{F}_\uparrow e^{-jk2d\cos\theta}$

so that

(B-7) $\hat{\underline{E}}_2 = (\underline{u}_x \cos\theta - \underline{u}_z \sin\theta)\, \hat{F}_\uparrow e^{-jk(x\sin\theta + z\cos\theta)}$

$+ (\underline{u}_x \cos\theta + \underline{u}_z \sin\theta)\, (-\hat{F}_\uparrow e^{-jk2d\cos\theta})$

$\cdot e^{-jk(x\sin\theta - z\cos\theta)}$

---

*Note that we assume the properties of Regions 1 and 2 to be
identical. A dielectric-filled region would require modification
of the equations but would yield similar results.

and

(B-8) $\hat{\underline{E}}_2\Big|_{z=0} = (\underline{u}_x \cos\theta - \underline{u}_z \sin\theta) \hat{F}_\uparrow e^{-jkx \sin\theta}$

$$-(\underline{u}_x \cos\theta + \underline{u}_z \sin\theta) \hat{F}_\uparrow e^{-jk2d \cos\theta} e^{-jkx \sin\theta}$$

Now at $z = 0$ we have a very thin sheet of high but finite conductivity. Consider a slab of this material as shown in Figure B-3. For the electric field

(B-9) $\oint \hat{\underline{E}} \cdot \underline{d\ell} = -j\omega\mu \int_s \hat{\underline{H}} \cdot \underline{ds}_H$

(B-10) $\int_0^L \hat{E}_{1t} dx + \int_0^{z_0} \hat{E}_{2n} dz - \int_L^0 \hat{E}_{2t} dx - \int_{z_0}^0 \hat{E}_{2n} dz$

$$= -j\omega\mu \int_0^{z_0} \int_0^L \hat{H}_t(z) dx dz$$

FIGURE B-3
SEGMENT OF CURRENT SHEET
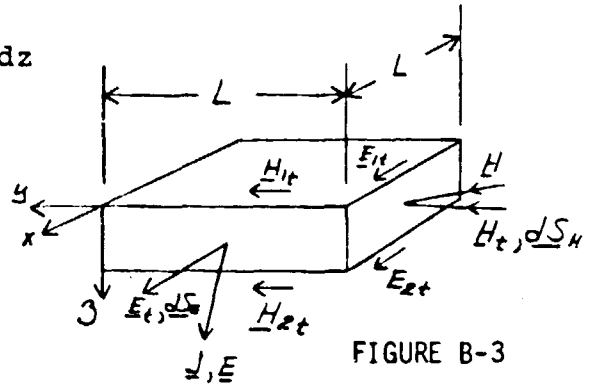
In the limit at $z_0 \to 0$

(B-11) $L (\hat{E}_{1t} - \hat{E}_{2t}) = -j\omega\mu L \int_0^{z_0} \hat{H}_t(z) dz = 0$

Therefore,

(B-12) $E_{1t}\Big|_{z=0} = E_{2t}\Big|_{z=0} = \hat{F}_\uparrow \cos (1 - e^{-jk2d \cos\theta}) e^{-jkx \sin\theta}$

Still considering the high conductivity sheet, the square slab shown has a resistance (for x-directed currents)

(B-13) $R_0 = \dfrac{L}{\sigma A} = \dfrac{L}{\sigma L z_0} = \dfrac{1}{\sigma z_0}$ so that $\sigma = \dfrac{1}{R_0 z_0}$

(B-14) $\oint \hat{\underline{H}} \cdot \underline{d\ell} = (\sigma + j\omega\epsilon_1) \oint_s \hat{\underline{E}} \cdot \underline{ds}_E$

-50-

(B-15) $\int_{-L}^{o} \hat{H}_{1t} dy + \int_{o}^{z_o} \hat{H}_n dz + \int_{o}^{-L} \hat{H}_{2t} dy - \int_{z_o}^{o} \hat{H}_n dz$

$$= (\frac{1}{R_o z_o} + j\omega\epsilon_1) \int_s \underline{\hat{E}} \cdot \underline{ds}_E$$

In the limit as $z_o \to 0$ (R_o constant)

(B-16) $L(\hat{H}_{1t} - \hat{H}_{2t}) = \frac{1}{R_o z_o} \int_s \underline{\hat{E}} \cdot \underline{ds}_E$

$$= \frac{1}{R_o z_o} \int_o^{z_o} \int_o^L \hat{E}_t(z) \, dydz$$

Cancelling L and applying L'Hospital's rule,

(B-17) $\hat{H}_{1t} - \hat{H}_{2t} = \lim_{z_o \to 0} \dfrac{\dfrac{d}{dz_o} \int_o^{z_o} \hat{E}_t(z)dz}{\dfrac{d}{dz_o} R_o z_o}$

$$= \frac{\hat{E}(z_o)}{R_o} \Big|_{z_o = 0}$$

$$= \frac{\hat{E}_t(0)}{R_o}$$

Examining the tangential components at $z = 0$ yields

$\underline{\hat{E}}$: $\underline{u}_x \cos\theta \, (\hat{A}_\uparrow + \hat{B}_\uparrow)e^{-jkx \sin\theta}$

$\qquad -\underline{u}_x \cos\theta \, \hat{F}_\uparrow (1 - e^{-jk2d \cos\theta})e^{-jkx \sin\theta} \underset{\equiv}{x,y} 0$

(B-19) $\hat{A}_\uparrow + \hat{B}_\uparrow = \hat{F}_\uparrow (1 - e^{-jk2d \cos\theta})$

$$\underline{H}: \ \underline{u}_y \ \eta^{-1}(\hat{A}_\uparrow - \hat{B}_\uparrow)e^{-jkx \sin\theta}$$

$$-\underline{u}_y \ \eta^{-1} \ \hat{F}_\uparrow (1 - e^{-jk2d \cos\theta}) \ e^{-jkx \sin\theta}$$

$$\overset{x,y}{\equiv} \ \underline{u}_y \cos\theta \ \frac{\hat{F}_\uparrow}{R_o} (1 - e^{-jk2d \cos\theta})e^{-jkx \sin\theta}$$

(B-20) $\quad \hat{A}_\uparrow - \hat{B}_\uparrow = \hat{F}_\uparrow \left[(1 + e^{-jk2d \cos\theta}) + \frac{\eta}{R_o} \cos\theta \ (1 - e^{-jk2d \cos\theta}) \right]$

From Equation (B-19)

(B-19') $\quad \hat{F} = \dfrac{\hat{A}_\uparrow + \hat{B}_\uparrow}{1 - e^{-jk2d \cos\theta}}$

so that

(B-20') $\quad \hat{A}_\uparrow - \hat{B}_\uparrow = (\hat{A}_\uparrow + \hat{B}_\uparrow) \left[\dfrac{1 + e^{-jk2d \cos\theta}}{1 - e^{-jk2d \cos\theta}} + \dfrac{\eta}{R_o} \cos\theta \right]$

from which

(B-21) $\quad \hat{\rho}_\uparrow = \dfrac{\hat{B}_\uparrow}{\hat{A}_\uparrow} = - \dfrac{(\frac{\eta}{R_o} \cos\theta - 1) + j \cot (\frac{2\pi}{\lambda}d \cos\theta)}{(\frac{\eta}{R_o} \cos\theta + 1) + j \cot (\frac{2\pi}{\lambda}d \cos\theta)}$

PERPENDICULAR POLARIZATION

Applying essentially the same approach to perpendicular polarization yields:

For Region 1 (z < 0):

(B-22) $\quad \hat{\underline{E}}_1 = \underline{u}_y \left[\hat{A}_\rightarrow e^{-jk(x \sin\theta + z \cos\theta)} - \hat{B}_\rightarrow e^{-jk(x \sin\theta - z \cos\theta)} \right]$

(B-23) $\hat{\underline{H}}_1 = \eta^{-1} \left[(-\underline{u}_x \cos\theta + \underline{u}_z \sin\theta) \hat{A}_\rightarrow e^{-jk(x \sin\theta + z \cos\theta)} \right.$

$$\left. + (-\underline{u}_x \cos\theta - \underline{u}_z \sin\theta) \hat{B}_\rightarrow e^{-jk(x \sin\theta - z \cos\theta)} \right]$$

For Region 2 (0 < z < d):

(B-24) $\hat{\underline{E}}_2 = \underline{u}_y \left[\hat{F}_\rightarrow e^{-jk(x \sin\theta + z \cos\theta)} - \hat{G}_\rightarrow e^{-jk(x \sin\theta - z \cos\theta)} \right]$

(B-25) $\hat{\underline{H}}_2 = \eta^{-1} \left[(-\underline{u}_x \cos\theta + \underline{u}_x \sin\theta) \hat{F}_\rightarrow e^{-jk(x \sin\theta + z \cos\theta)} \right.$

$$\left. + (-\underline{u}_x \cos\theta - \underline{u}_x \sin\theta) \hat{G}_\rightarrow e^{-jk(x \sin\theta - z \cos\theta)} \right]$$

At z = d, $\hat{\underline{E}}_t = 0$. Therefore,

(B-26) $\underline{u}_y (\hat{F}_\rightarrow e^{-jkd \cos\theta} - \hat{G}_\rightarrow e^{+jkd \cos\theta}) e^{-jkx \sin\theta} \underset{x,y}{\equiv} 0$

(B-26') $\hat{G}_\rightarrow = + \hat{F}_\rightarrow e^{-jk2kd \cos\theta}$

and thus

(B-27) $\hat{\underline{E}}_2 = \underline{u}_y \hat{F}_\rightarrow \left[e^{-jk(x \sin\theta + z \cos\theta)} \right.$

$$\left. - e^{-j2kd \cos\theta} e^{-jk(x \sin\theta - z \cos\theta)} \right]$$

(B-28) $\hat{\underline{E}}_2 \bigg|_{z = 0} = \underline{u}_y \hat{F}_\rightarrow \left[1 - e^{-j2kd \cos\theta} \right] e^{-jkx \sin\theta}$

(B-29) $\hat{H}_{1t} - \hat{H}_{2t} = \dfrac{-\hat{E}_t(0)}{R_o}$

$$= - \dfrac{\hat{F}_\rightarrow}{R_o} e^{-jkx \sin\theta} (1 - e^{-jk2d \cos\theta})$$

Examining tangential components at z = 0 gives us

-53-

(B-30) $\quad \hat{\underline{E}}: \ \underline{u}_y \left[\hat{A}_\rightarrow - \hat{B}_\rightarrow \right] e^{-jkx \ \sin\theta} \ -\underline{u}_y \hat{F}_\rightarrow \left[1 - e^{-j2kd \ \cos\theta} \right] e^{-jkx \ \sin\theta} \ \overset{x,y}{\equiv} 0$

(B-31) $\quad \hat{A}_\rightarrow - \hat{B}_\rightarrow = \hat{F}_\rightarrow \left[1 - e^{-jk2d \ \cos\theta} \right]$

(B-32) $\quad \hat{\underline{H}}: \ -\underline{u}_x \ \eta^{-1} (\hat{A}_\rightarrow + \hat{B}_\rightarrow) \cos\theta \ e^{-jkx \ \sin\theta}$

$$+ \ \underline{u}_x \ \eta^{-1} \ \hat{F}_\rightarrow (1 + e^{-jk2d \ \cos\theta}) e^{-jkx \ \sin\theta}$$

$$\overset{x,y}{\equiv} \ -\underline{u}_x \ \frac{\hat{F}_1}{R_o} \left[1 - e^{-jk2d \ \cos\theta} \right] e^{-jkx \ \sin\theta}$$

(B-33) $\quad (\hat{A}_\rightarrow + \hat{B}_\rightarrow) \ \cos\theta = \hat{F}_\rightarrow \left[(1 + e^{-jk2d \ \cos\theta}) \cos\theta + \frac{\eta}{R_o} (1 - e^{-jk2d \ \cos\theta}) \right]$

from which

$$(B-34) \quad \hat{\rho}_\rightarrow = \frac{\hat{B}_\rightarrow}{\hat{A}_\rightarrow} = \frac{\left| \dfrac{\eta}{R_o} \ \sec\theta - 1 \right| - j \cot \left[\dfrac{2\pi}{\lambda} d \ \cos\theta \right]}{\left[\dfrac{\eta}{R_o} \ \sec\theta + 1 \right] - j \cot \left[\dfrac{2\pi}{\lambda} d \ \cos\theta \right]}$$

For easy comparison to Jasik[5] we define

$$M_\uparrow \cdot \equiv \cdot \frac{\eta}{R_o} \ \cos\theta \quad \text{and} \quad M_\rightarrow \cdot \equiv \cdot \ \frac{\eta}{R_o} \ \sec\theta$$

and rewrite

$$2kd \ \cos\theta = \frac{\pi}{2} \frac{\lambda_0}{\lambda} \ \cos\theta; \quad d = \frac{\lambda_0}{4}; \quad \eta = \sqrt{\frac{\mu}{\epsilon}} = 377$$

so that

$$(B-21') \quad \hat{\rho}_\uparrow = \frac{\hat{B}_\uparrow}{\hat{A}_\uparrow} = - \ \frac{(M_\uparrow - 1) + j \cot \left(\dfrac{2\pi}{\lambda} d \ \cos\theta \right)}{(M_\uparrow - 1) + j \cot \left(\dfrac{2\pi}{\lambda} d \ \cos\theta \right)}$$

$$(B-35) \quad |\hat{\rho}_\uparrow|^2 = \frac{(M_\uparrow - 1)^2 + \cot^2 \left(\dfrac{\pi}{2} \dfrac{\lambda_0}{\lambda} \ \cos\theta \right)}{(M_\uparrow + 1)^2 + \cot^2 \left(\dfrac{\pi}{2} \dfrac{\lambda_0}{\lambda} \ \cos\theta \right)}$$

and

$$(B-34') \quad \hat{\rho}_{\rightarrow} = \frac{\hat{B}_{\rightarrow}}{\hat{A}_{\rightarrow}} = \frac{(M_{\rightarrow} - 1) - j \cot (\frac{2\pi}{\lambda} d \cos\theta)}{(M_{\rightarrow} + 1) - j \cot (\frac{2\pi}{\lambda} d \cos\theta)}$$

$$(B-36) \quad |\hat{\rho}_{\rightarrow}|^2 = \frac{(M_{\rightarrow} - 1)^2 + \cot^2 (\frac{\pi \lambda_0}{2\lambda} \cos\theta)}{(M_{\rightarrow} + 1)^2 + \cot^2 (\frac{\pi \lambda_0}{2\lambda} \cos\theta)}$$

Returning to a notation convenient to our purposes,

$$(B-21) \quad \hat{\rho}_{\uparrow} = - \frac{(\frac{\eta}{R_o} \cos\theta - 1) + j \cot (\frac{2\pi}{\lambda} d \cos\theta)}{(\frac{\eta}{R_o} \cos\theta + 1) + j \cot (\frac{2\pi}{\lambda} d \cos\theta)}$$

and

$$(B-34) \quad \rho_{\rightarrow} = \frac{(\frac{\eta}{R_o} \sec\theta - 1) - j \cot (\frac{2\pi}{\lambda} d \cos\theta)}{(\frac{\eta}{R_o} \sec\theta + 1) - j \cot (\frac{2\pi}{\lambda} d \cos\theta)}$$

Equations (B-21) and (B-34) provide confirmation of, and
limitations on, the corresponding expressions in Jasik
and provide a measure of scatter when deviations from
design conditions occur. This effort has also led to a
previously unexpected result. Setting the various real
and imaginary parts of the numerators of Equations (B-21)
and (B-34) equal to zero reveals that total absorption
is possible at angles off normal ($\theta \neq 0^\circ$):

$$(B-37) \quad \uparrow: \frac{\eta}{R_o} \cos\theta - 1 = 0$$

and

$$(B-38) \quad \cot (\frac{2\pi}{\lambda} d \cos\theta) = 0$$

or

(B-39)   †: $\frac{\eta}{R_o} \sec\theta - 1 = 0$

and

(B-40) $\cot \left(\frac{2\pi}{\lambda} d \cos\theta\right) = 0$

$$\frac{2\pi}{\lambda} d \cos\theta = \frac{\pi}{2}, \frac{3\pi}{2}, \frac{5\pi}{2}, \cdots$$

That is,

(B-41) $d = (2n - 1) \frac{\lambda}{4} \sec\theta \qquad n = 1,2,3,\ldots$

and

(B-42) $R_o = \eta \cos\theta$ for parallel polarization

or

(B-43) $R_o = \eta \sec\theta$ for perpendicular polarization

Equations (B-41) and either (B-42) or (B-43) describe physical conditions on d and R_o for any given angle and wavelength to provide the results illustrated in Figure B-4. (Compare to Figure B-2).
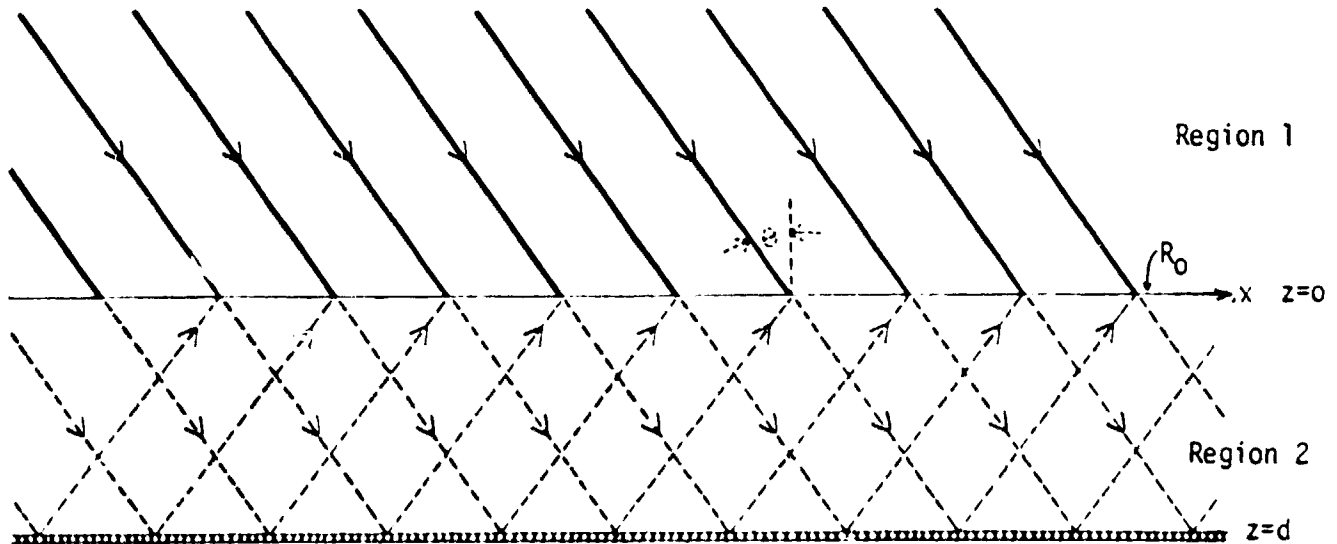
FIGURE B-4

CURRENT SHEET MODEL
CROSS-SECTION: MATCHED CASE

-56-

APPENDIX C

WAVEGUIDE MODEL

WAVEGUIDE MODEL

While the CSM provides several insights into the functioning of the Rectenna and suggests some useful modifications of the Reference Design, it provides neither clear criteria for element spacing nor characteristics of the near field. Therefore, a second model is needed, one which will quantify the electromagnetic modes (field configurations) in the immediate vicinity of Rectenna element. The Waveguide Model, based on properties of a special waveguide described by Wheeler[9] in his analysis of a large planar array, characterizes EM modes generated by planar waves normal to the array. It should be understood that this model will apply only to incidence normal to the array.

Specifically, the waveguide has special "imaging" characteristics due to its special nature. Unlike a conventional waveguide, two opposite walls of the rectangle are "magnetic" and non-conductive ($\mu = \infty$, $\sigma = 0$); the other two walls are perfectly conducting ($\sigma = \infty$).

To examine the reflective behavior of the individual walls, we apply Equations (B-1) through (B-4) to a general interface between two semi-infinite regions (See Figure C-1). Because
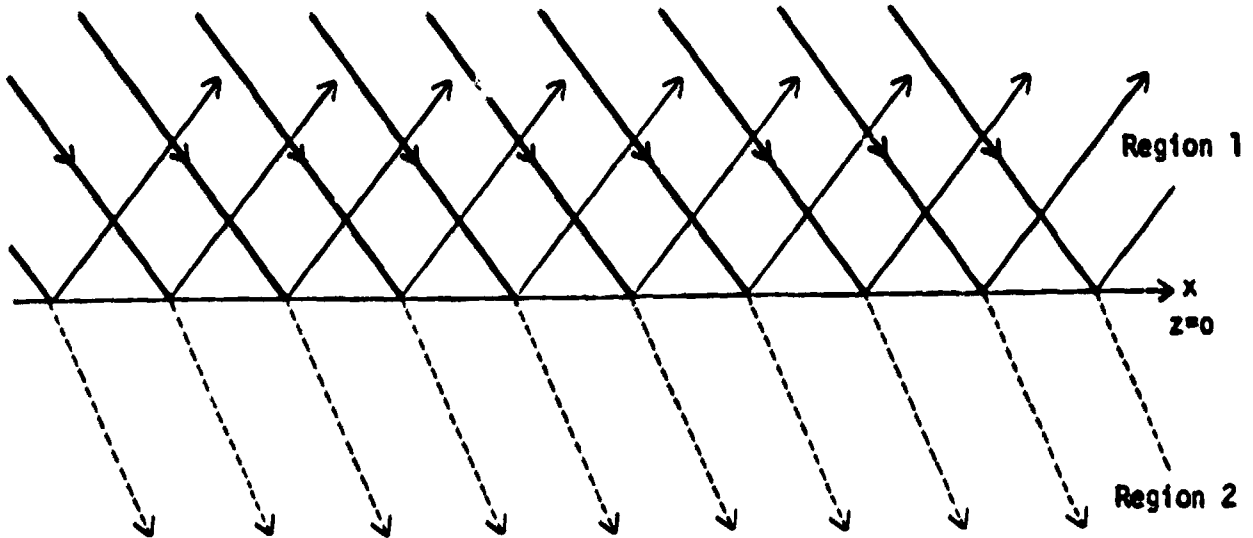
FIGURE C-1

A PLANE WAVE AT A PLANAR INTERFACE

Region 2 is semi-infinite

$$G_\uparrow \equiv 0$$

and we have for Region 1 (z < 0):

$$(B-1') \quad \hat{\underline{E}}_1 = (\underline{u}_x \cos\theta_1 - \underline{u}_z \sin\theta_1) \, \hat{A}_\uparrow e^{-jk(x\sin\theta_1 + z\cos\theta_1)}$$

$$+ (\underline{u}_x \cos\theta_1 + \underline{u}_z \sin\theta) \, \hat{B}_\uparrow e^{-jk_1(x\sin\theta_1 - z\cos\theta_1)}$$

$$(B-2') \quad \hat{\underline{H}}_1 = \underline{u}_y \, \eta_1^{-1} \left[\hat{A}_\uparrow e^{-jk_1(x\sin\theta_1 + z\cos\theta_1)} - B_\uparrow e^{-jk_1(x\sin\theta_1 - z\cos\theta_1)} \right]$$

Similarly, for Region 2 (0 < z < d)

$$(B-3') \quad \hat{\underline{E}}_2 = (\underline{u}_x \cos\theta_2 - \underline{u}_z \sin\theta_2) \, \hat{F}_\uparrow e^{-jk_2(x\sin\theta_2 + z\cos\theta_2)}$$

$$(B-4') \quad \hat{\underline{H}}_2 = \underline{u}_y \, \eta_2^{-1} \, \hat{F}_\uparrow e^{-jk_2(x\sin\theta_2 + z\cos\theta_2)}$$

At the interface (z = 0) tangential components must match. Thus,

(C-1) $\hat{\underline{E}}$: $\underline{u}_x \cos\theta \quad (\hat{A}_\uparrow + \hat{B}_\uparrow)e^{-jk_1 x\sin\theta_1}$

$$\underset{z}{\overset{x,y}{}} \quad \underline{u}_x \cos\theta_2 \; \hat{F}_\uparrow e^{-jk_2 x\sin\theta_2}$$

and so

(C-2) $\quad k_1\sin\theta_1 = k_2\sin\theta_2 \qquad$ (Snell's Law of Refraction)

and

(C-3) $\quad (\hat{A}_\uparrow + \hat{B}_\uparrow) \cos\theta_1 = \hat{F}_\uparrow\cos\theta_2$

(C-4) $\hat{\underline{H}}$: $\quad \underline{u}_y \eta_1^{-1}(\hat{A}_\uparrow - \hat{B}_\uparrow) \; e^{-jk_1 x\sin\theta_1}$

$$\underset{z}{\overset{x,y}{}} \quad \underline{u}_y \eta_2^{-1}\hat{F}_\uparrow e^{-jk_2 x\sin\theta_2}$$

(C-5) $\quad \eta_2(\hat{A}_\uparrow - \hat{B}_\uparrow) = \eta_1\hat{F}_\uparrow$

(C-6) $\quad (\hat{A}_\uparrow + \hat{B}_\uparrow) \cos\theta_1 = \dfrac{\eta_2(\hat{A}_\uparrow - \hat{B}_\uparrow) \cos\theta_2}{\eta_1}$

(C-7) $\quad \hat{B}_\uparrow \left[\cos\theta_1 + \dfrac{\eta_2}{\eta_1} \cos\theta_2 \right] = \hat{A}_\uparrow \left[\dfrac{\eta_2}{\eta_1} \cos\theta_2 - \cos\theta_1 \right]$

(C-8) $\quad \dfrac{\hat{B}_\uparrow}{\hat{A}_\uparrow} = \dfrac{\eta_2\cos\theta_2 - \eta_1\cos\theta_1}{\eta_2\cos\theta_2 + \eta_1\cos\theta_1}$

Let us first consider the familiar result of an ideal conductor characterized by

(C-9) $\quad \underset{\substack{\epsilon_2 \to \infty \\ (\sigma_2 \to \infty)}}{\text{Lim}} \dfrac{\hat{B}_\uparrow}{\hat{A}_\uparrow} = -1$

so that the electric field in Region 1 becomes

(C-10) $\quad \hat{\underline{E}}_1 = (\underline{u}_x \cos\theta - \underline{u}_z \sin\theta_1) \hat{A}_\uparrow e^{-jk (x\sin\theta_1 - z \cos\theta_1)}$

$$+ (\underline{u}_x \cos\theta_1 + \underline{u}_z \sin\theta_1) (-\hat{A}_\uparrow)e^{-jk_1(x\sin\theta_1 - z \cos\theta_1)}$$

This tells us that the images are as in Figure C-2.
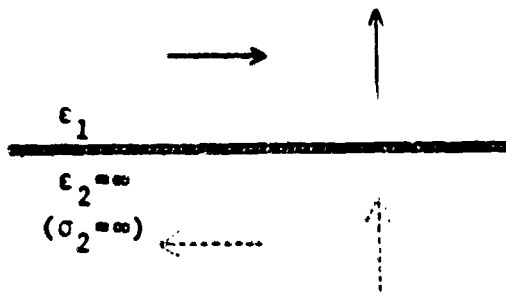
FIGURE C-2

IMAGING AT AN IDEAL
CONDUCTING WALL
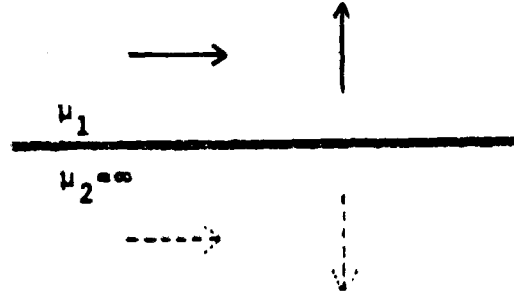
FIGURE C-3

IMAGING AT AN IDEAL MAGNETIC WALL

Similarly, for an ideal magnetic material for which σ_2 is finite

$$(\text{C-11}) \quad \lim_{\mu_2 \to \infty} \frac{B_\uparrow}{A_\uparrow} = +1$$

Leading us to

$$(\text{C-12}) \quad \hat{\underline{E}}_1 = (\underline{u}_x \cos\theta_1 - \underline{u}_z \sin\theta_1) \, \hat{A}_\uparrow e^{-jk_1(x\sin\theta_1 + z\cos\theta_1)}$$

$$+ (\underline{u}_x \cos\theta_1 + \underline{u}_z \sin\theta_1) \, (+\hat{A}_\uparrow) e^{-jk_1(x\sin\theta_1 - z\cos\theta_1)}$$

so that the images are as shown in Figure C-3. The results
of Equations (C-10) and (C-12) suggest that we can usefully
conceive of a "mixed wall" waveguide such as is shown in Figure
C-4. (We impose $\sigma = 0$ on the magnetic walls for later convenience.)
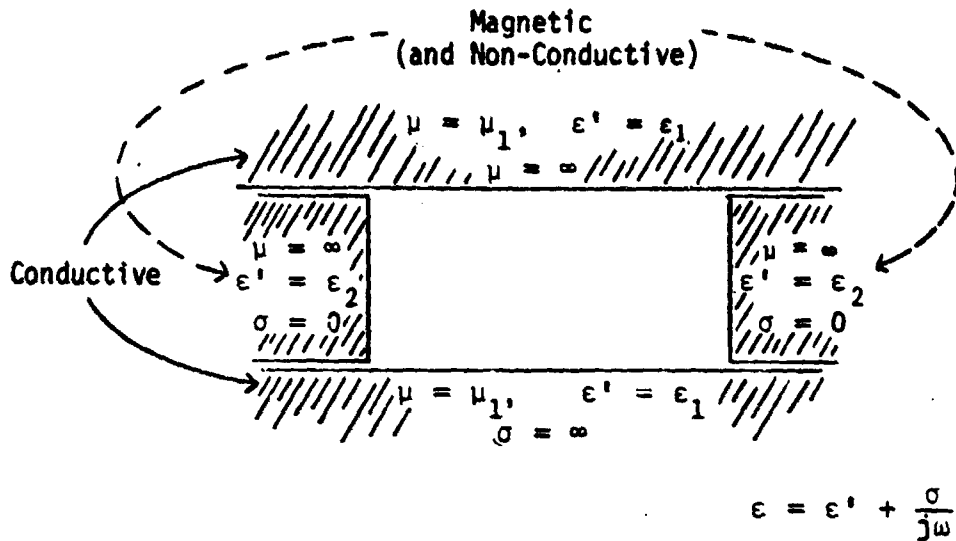
FIGURE C-4

CROSS-SECTION, MIXED-WALL WAVEGUIDE

If such a waveguide has a probe (monopole antenna) inserted through one of the conductive walls, the probe will have images such as are shown in Figure C-5.
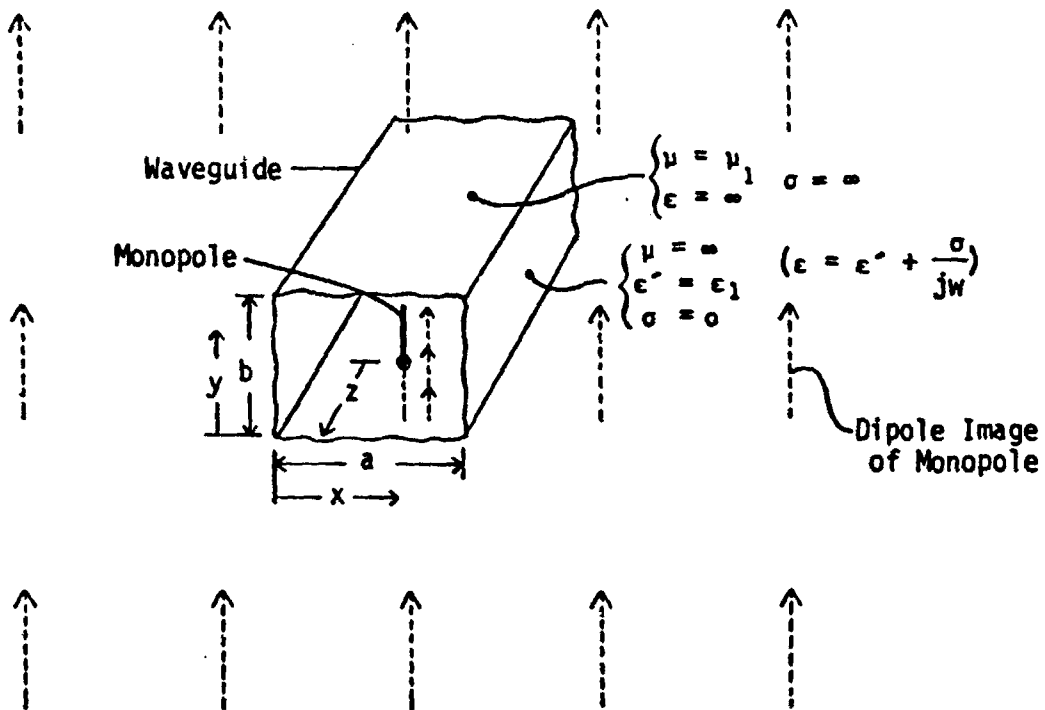
FIGURE C-5

IMAGING PROPERTIES OF MIXED-WALL
WAVEGUIDE WITH MONOPOLE

The array of images is of infinite extent, and the single monopole in the mixed-wall waveguide is equivalent to an infinite array of perfectly spaced dipoles all excited identically. Or, as in Figure C-6, we may claim that an infinite array of identically excited dipoles could have infinitely thin walls forming mixed wall waveguides erected between them without altering the field pattern.
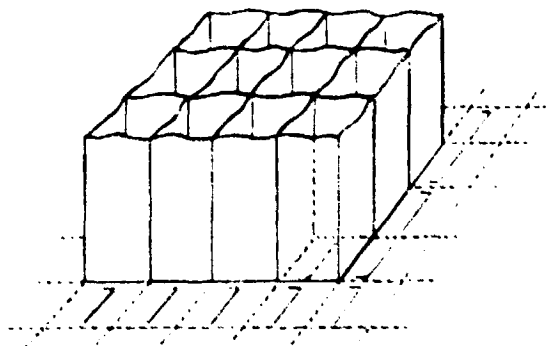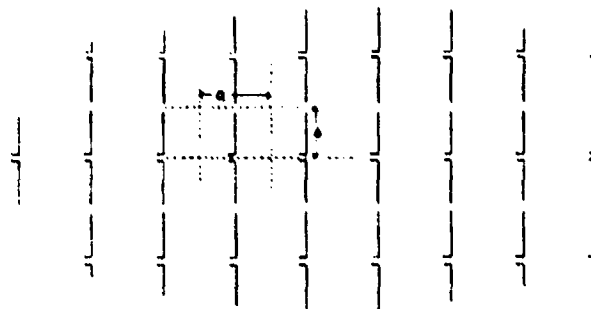
FIGURE C-6   FIGURE C-7

FIGURES C-6, C-7

ARRAY SECTIONED BY MIXED-WALL WAVEGUIDES

This concept, then, provides us a method of examining the field patterns within any one waveguide and claiming with confidence that we know the patterns everywhere above the equivalent infinite array of dipoles. The applicability

of such a scheme, of course, depends upon the correspondence of the infinite extent model of the real Rectenna array and on a restriction to normal incidence. A more intuitive discussion of the waveguide model is given on page 17.

To examine the field patterns within the mixed wall waveguide we return once again to the wave equations in $\underline{\hat{E}}$ and $\underline{\hat{H}}$, Equations (A-5) and (A-6). We will find it convenient to define the waveguide such that the z-axis is the direction of propagation—that is, the axial dimension of the waveguide as shown in Figure C-5. We can then decompose the Laplacian (∇^2) operator as

$$(C-13) \qquad \nabla^2 \underline{\hat{E}} = \nabla^2_{xy} \underline{\hat{E}} + \frac{\partial^2}{\partial^2_z} \underline{\hat{E}}$$

For + z propagation

$$(C-14) \qquad \underline{\hat{E}}(x,y,z,j\omega) = \underline{\dot{\hat{E}}}(x,y,j\omega)e^{-\gamma z}$$

and thus Equation (A-5) becomes

$$(C-15) \qquad \nabla^2 \underline{\dot{\hat{E}}} = \nabla^2_{xy} \underline{\dot{\hat{E}}} + \gamma^2 \underline{\dot{\hat{E}}} = -\omega^2 \mu\epsilon \underline{\dot{\hat{E}}}$$

$$(C-16) \qquad \nabla^2_{xy} \underline{\dot{\hat{E}}} = -(\omega^2\mu\epsilon + \gamma^2)\,\underline{\dot{\hat{E}}}$$

$$= -k^2_c \underline{\dot{\hat{E}}}$$

where $k^2_c = \omega^2_c \mu\epsilon = \omega^2\mu\epsilon + \gamma^2$ k_c is the "cutoff wavenumber", and ω_c is the "cutoff frequency".

Similarly, Equation (A-6) becomes

(C-17) $\quad \nabla^2_{xy} \, \dot{\underline{\hat{H}}} = - k^2_c \, \dot{\underline{\hat{H}}}$

We will also need, from Equations (A-1) and (A-2),

(C-18) $\quad \dot{\hat{H}}_x = k^{-2}_c \left[j\omega\varepsilon \frac{\partial}{\partial y} \dot{\hat{E}}_z - \gamma \frac{\partial}{\partial x} \dot{\hat{H}}_z \right]$

(C-19) $\quad \dot{\hat{H}}_y = -k^{-2}_c \left[j\omega\varepsilon \frac{\partial}{\partial x} \dot{\hat{E}}_z + \gamma \frac{\partial}{\partial y} \dot{\hat{H}}_z \right]$

(C-20) $\quad \dot{\hat{E}}_x = -k^{-2}_c \left[\gamma \frac{\partial}{\partial x} \dot{\hat{E}}_z + j\omega\mu \frac{\partial}{\partial y} \dot{\hat{H}}_z \right]$

(C-21) $\quad \dot{\hat{E}}_y = k^{-2}_c \left[\gamma \frac{\partial}{\partial y} \dot{\hat{E}}_z + j\omega\mu \frac{\partial}{\partial x} \dot{\hat{H}}_z \right]$

As is usual with an "ordinary" waveguide, we will decompose the field into the various possible modes which could exist alone or in combination within the bounded region. There are two major classes of such modes--the TM and the TE (transverse magnetic and tranverse electric), with the additional possibility of two orthogonal TEM (transverse electric and magnetic*) modes.

For TM_{fg} modes ($H_z = 0$)

(C-16') $\quad \nabla^2_{xy} \, \dot{\hat{E}}_z = -k^2_c \, \dot{\hat{E}}_z$

yields

(C-22) $\quad \dot{\hat{E}}_z = (\hat{A} \cos px + \hat{B} \sin px)(\hat{C} \cos qy + \hat{D} \sin qy)$

where $p^2 + q^2 = k^2_c$

---

*Often read as "Transverse Electromagnetic". These are non-existent in an ordinary hollow waveguide. As will be shown, one TEM is not only possible but quite significant here.

Consideration of the (conductive) boundaries at

$$y = 0 \text{ and } y = b$$

tells us that

$$\hat{C} = 0$$

and

$$q = \frac{g\pi}{b} \quad g = 1,2,3,\ldots \text{(note that g may not be zero)}$$

From Equation (C-19)

(C-23) $\hat{H}_y = \frac{j\omega\epsilon p}{k_c^2} (-\hat{A} \sin px + \hat{B} \cos px) (D \sin qy)$

Consideration of the (magnetic) boundaries at

$$x = 0 \text{ and } x = a$$

tells us that

$$\hat{B} = 0$$

and

$$p = \frac{f\pi}{a} \quad f = 0,1,2,3,\ldots$$

so that

(C-24) $\dot{\hat{E}}_z = \hat{B}_{fg} \cos px \sin qy \qquad B_{fg} = AD$

(C-25) $\dot{\hat{H}}_x = \frac{j\omega\epsilon q}{k_c^2} \hat{B}_{fg} \cos px \cos qy$

(C-26) $\dot{\hat{H}}_y = \frac{j\omega\epsilon p}{k_c^2} \hat{B}_{fg} \sin px \sin qy$

(C-27) $\dot{\hat{E}}_x = \frac{\gamma p}{k_c^2} \hat{B}_{fg} \sin px \sin qy$

(C-28) $\dot{\hat{E}}_y = - \frac{\gamma q}{k_c^2} \hat{B}_{fg} \cos px \cos qy$

-67-

Similarly for TE$_{mn}$ modes (E$_z$ = 0)

(C-29) $\overset{\bullet}{\hat{H}}_z = \hat{A}_{mn} \sin px \cos qy$

(C-30) $\overset{\bullet}{\hat{H}}_x = - \frac{\gamma p}{k_c^2} \hat{A}_{mn} \cos px \cos qy$

(C-31) $\overset{\bullet}{\hat{H}}_y = \frac{\gamma q}{k_c^2} \hat{A}_{mn} \sin px \sin qy$

(C-32) $\overset{\bullet}{\hat{E}}_x = \frac{j\omega\varepsilon q}{k_c^2} \hat{A}_{mn} \sin px \sin qy$

(C-33) $\overset{\bullet}{\hat{E}}_y = \frac{j\omega\varepsilon p}{k_c^2} A_{mn} \cos px \cos qy$

in which $q = \frac{n\pi}{b}$ may be zero but $p = \frac{m\pi}{a}$ may not be zero.

Before going further, let us consider the possibilities of TEM modes (E$_z$ ≡ H$_z$ ≡ 0). For this mode to propagate energy in the z direction it is necessary to have the pairs, $\hat{E}_x$, $\hat{H}_y$ and/or $\hat{E}_y$, $\hat{H}_x$. Equations (A-1) and (A-2) require that these may be non-zero when $\hat{E}_z$ and $\hat{H}_z$ are both zero only if $\hat{E}_x$, $\hat{E}_y$, $\hat{H}_x$, and $\hat{H}_y$ are non-varying with x and y. This requirement, along with the boundaries, eliminates the $\hat{E}_x$, $\hat{H}_y$ pair. However, unlike the ordinary closed waveguide, the boundaries do not forbid the $\hat{E}_y$, $\hat{H}_x$ case. Thus, we have a waveguide capable of supporting a TEM mode. This was a necessary conclusion if our model was to represent the infinite array, since the TEM mode corresponds exactly to the plane wave which we know will be generated by the array of dipoles and which is our

desired wave. In fact, what we actually wish to demonstrate
is that spacings of dipoles (dimensions of the waveguide)
exist for which none of the other modes will propagate. Under
such conditions these other modes will be present reactively
and will be the necessary "near field" components which "make
up the difference" between the discrete dipoles of the actual
array and the continuous current in the current sheet model
of Appendix B.

To this end we will now consider the dimensional require-
ments for these higher (TM and TE) modes to propagate. Recall
from the derivation of Equation (C-16) and from Equation (C-22)
that

(C-34) $\quad k_c^2 = \omega_c^2 \mu\epsilon = p^2 + q^2 = (\frac{m\pi}{a})^2 + (\frac{n\pi}{b})^2$

so that

(C-35) $\quad f_c = \frac{1}{2\pi\sqrt{\mu\epsilon}} \sqrt{(\frac{m\pi}{a})^2 + (\frac{n\pi}{b})^2}$

$\qquad = \frac{c}{2} \sqrt{(\frac{m}{a})^2 + (\frac{n}{b})^2}$

For a wave to propagate, the propagation constant γ as
defined in Equation (C-14) must be predominantly* imaginary.
Since, by the definition of k_c,

───────────────

*In the lossless idealization at hand, γ will be purely imaginary
or purely real since losses cause it to be a general complex
number in an ordinary waveguide.

(C-36) $\quad \gamma = \sqrt{k_c^2 - \omega^2 \mu \epsilon}$

$$= \sqrt{\omega_c^2 \mu \epsilon - \omega^2 \mu \epsilon}$$

$$= \frac{2\pi}{c} \sqrt{f_c^2 - f^2}$$

it is apparent that for

$$f > f_c$$

γ is imaginary and the mode propagates, and for

$$f < f_c$$

γ is real and the mode is evanescent (reactive, non-propagating, cut off).

Of course, we are interested in the inverse problem here. That is, we are dealing with a fixed frequency and wish to determine dimensions which establish the transition (cut off) between propagation and evanescence. Since

$$f_c < f$$

$$\frac{c}{2} \sqrt{\left(\frac{m}{a}\right)^2 + \left(\frac{n}{b}\right)^2} < f.$$

$$\frac{\lambda}{2} \sqrt{\left(\frac{m}{a}\right)^2 + \left(\frac{n}{b}\right)^2} < 1$$

yielding

$$\left(\frac{m\lambda}{2a}\right)^2 + \left(\frac{n\lambda}{2b}\right)^2 < 1$$

We will now apply these conditions to the modes with the lower values of indices (m, n, or f, g). When these are cut off, the higher orders will also clearly be cut off.

For the TE_{10} mode,

$$\hat{H}_z = \hat{A} \sin \frac{\pi}{a}x \, e^{-j\beta z}$$

$$\hat{E}_y = \frac{j\omega\mu\pi \hat{A}}{ak_c^2} \cos \frac{\pi}{a}x \, e^{-j\beta z}$$

$$\hat{H}_x = - \frac{j\beta\pi\hat{A}}{ak_c^2} \cos \frac{\pi}{a}x \, e^{-j\beta z}$$

where $j\beta = \gamma = \sqrt{k_c^2 - k^2}$ $k = 2\pi f\sqrt{\mu\epsilon} = \frac{2\pi}{\lambda}$

$$= \sqrt{(\frac{\pi}{a})^2 - k^2}$$

For the TM_{01} mode,

$$\hat{E}_z = \hat{B} \sin \frac{\pi}{b}y \, e^{-j\beta z}$$

$$\hat{H}_x = \frac{j\omega\epsilon\pi\hat{B}}{bk_c^2} \cos \frac{\pi}{b}y \, e^{-j\beta z}$$

$$\hat{E}_y = - \frac{j\beta\pi\hat{B}}{bk_c^2} \cos \frac{\pi}{b}y \, e^{-j\beta z}$$

where $j\beta = \gamma = \sqrt{k_c^2 - k^2}$ $k = 2\pi f\sqrt{\mu\epsilon} = \frac{2\pi}{\lambda}$

$$= \sqrt{(\frac{\pi}{b})^2 - k^2}$$

For the TE_{11} mode,

$$\hat{H}_z = \hat{A} \sin \frac{\pi}{a}x \cos \frac{\pi}{b}y \, e^{-j\beta z}$$

$$\hat{E}_x = \frac{j\omega\mu\pi\hat{A}}{bk_c^2} \sin\frac{\pi}{a}x \ \sin\frac{\pi}{b}y \ e^{-j\beta z}$$

$$\hat{E}_y = \frac{j\omega\mu\pi\hat{A}}{bk_c^2} \cos\frac{\pi}{a}x \ \cos\frac{\pi}{b}y \ e^{-j\beta z}$$

$$\hat{H}_x = \frac{j\beta\pi\hat{A}}{ak_c^2} \cos\frac{\pi}{a}x \ \cos\frac{\pi}{b}y \ e^{-j\beta z}$$

$$\hat{H}_y = \frac{j\beta\pi\hat{A}}{bk_c^2} \sin\frac{\pi}{a}x \ \sin\frac{\pi}{b}y \ e^{-j\beta z}$$

and for the TM_{11} mode,

$$\hat{E}_z = \hat{B} \cos\frac{\pi}{a}x \ \sin\frac{\pi}{b}y \ e^{-j\beta z}$$

$$\hat{E}_x = \frac{j\pi\beta\hat{B}}{ak_c^2} \sin\frac{\pi}{a}x \ \sin\frac{\pi}{b}y \ e^{-j\beta z}$$

$$\hat{E}_y = \frac{j\pi\beta\hat{B}}{bk_c^2} \cos\frac{\pi}{a}x \ \cos\frac{\pi}{b}y \ e^{-j\beta z}$$

$$\hat{H}_x = - \frac{j\omega\epsilon\pi\hat{B}}{bk_c^2} \cos\frac{\pi}{a}x \ \cos\frac{\pi}{b}y \ e^{-j\beta z}$$

$$\hat{H}_y = \frac{j\omega\epsilon\pi\hat{B}}{ak_c^2} \sin\frac{\pi}{a}x \ \sin\frac{\pi}{b}y \ e^{-j\beta z}$$

where $j\beta = \gamma = \sqrt{(\frac{\pi}{a})^2 + (\frac{\pi}{b})^2 - k^2}$ and $k = \frac{2\pi}{\lambda}$

for both TE_{11} and TM_{11} modes.

For the TE_{20},

$$\hat{H}_z = \hat{A} \sin\frac{2\pi}{a}x \ e^{-j\beta z}$$

$$\hat{E}_y = \frac{j\omega\mu 2\pi\hat{A}}{ak_c^2} \cos\frac{2\pi}{a}x \ e^{-j\beta z}$$

$$\hat{H}_x = \frac{j\beta\pi\hat{A}}{ak_c^2} \cos\frac{2\pi}{a}x \ e^{-j\beta z}$$

where $j\beta = \sqrt{(\frac{2\pi}{a})^2 - k^2}$ $\qquad k = \frac{2\pi}{\lambda}$

and $k_c = \frac{2\pi}{a}$

These results may be consolidated graphically as in Figure C-8 in which values of the dimensions "a" and "b" within the hashmarked region would cause all modes except the TEM and TE_{10} modes to be evanescent. Examination of
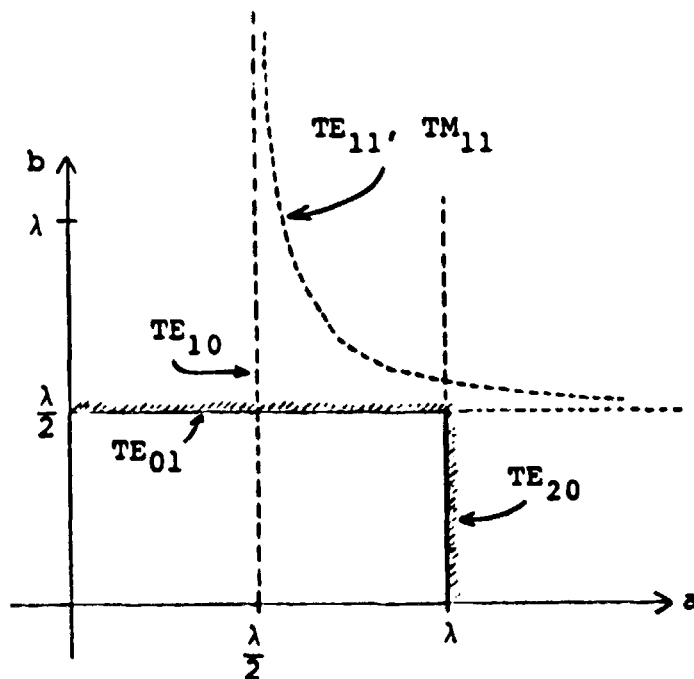
FIGURE C-8

CUTOFF LIMITS FOR LOWER
MODES IN MIXED-WALL WAVEGUIDE

the field configuration of the TE_{10} mode tells us that while this mode is "propagatable" it is not "generatable" by a probe at the $x = \frac{a}{2}$ location since that is a null point for the electric field. Since the model is valid only for ideally distributed and identically excited dipoles, there is no way the probe can fail to be at the $x = \frac{a}{2}$ position. (Note that "mode-hopping," the production of one mode from another due to imperfections, is not a problem here since we are dealing with an ideal waveguide.)

The total electric field, $\hat{\underline{E}}$, and the total magnetic field, $\hat{\underline{H}}$, in the mixed-wall waveguide are each sums of the various field configurations or modes that exist in the waveguide. Now $\hat{\underline{E}}$ and $\hat{\underline{H}}$ are vector and phasor sums of respective field components in the x, y, and z directions of Figure C-5. Thus for "+z propagating" field components, $\hat{\underline{E}}$ and $\hat{\underline{H}}$ can be represented by the equations given in Table I (page 75) where $\hat{A}_{mn}$ and $\hat{B}_{fg}$ are respectively the spatial maxima of $\hat{H}_z$ and $\hat{E}_z$ and where $\hat{K}_{oo}$ is the spatial maximum of the $\underline{H}$ field of the TEM wave. The α's and β's at the bottom of the table are respectively the real and imaginary parts of the expressions shown for the γ's. The terms involving double summations represent the "sums of the higher order modes". The leading terms in the equations for $\hat{E}_y$ and $\hat{H}_x$ are the equations for the TEM mode. If the higher order modes are evanescent (as is assumed), then the double summation terms are components of the fields associated with reactive power.

$$\hat{H}_z = 0 + \sum_{m=1}^{\infty}\sum_{n=0}^{\infty} \hat{A}_{mn} \sin\frac{m\pi x}{a}\cos\frac{n\pi y}{b}\, e^{-\alpha_{mn}z}$$

$$\hat{E}_z = 0 + \sum_{f=0}^{\infty}\sum_{g=1}^{\infty} \hat{B}_{fg}\cos\frac{f\pi x}{a}\sin\frac{g\pi y}{b}\, e^{-\alpha_{fg}z}$$

$$\hat{E}_x = 0 + \sum_{m=1}^{\infty}\sum_{n=0}^{\infty} \frac{j\omega\mu n\pi}{k_{cmn}^2 b}\hat{A}_{mn}\sin\frac{m\pi x}{a}\sin\frac{n\pi y}{b}\, e^{-\alpha_{mn}z}$$

$$+ \sum_{f=0}^{\infty}\sum_{g=1}^{\infty}\frac{-\alpha_{fg}f}{k_{cfg}^2 a}\hat{B}_{fg}\sin\frac{f\pi x}{a}\sin\frac{g\pi y}{b}\, e^{-\alpha_{fg}z}$$

$$\hat{E}_y = \frac{\mu}{\epsilon}\hat{K}_{oo}e^{-j\beta_{oo}z} + \sum_{m=1}^{\infty}\sum_{n=0}^{\infty}\frac{j\omega\mu m\pi}{k_{cmn}^2 a}\hat{A}_{mn}\cos\frac{m\pi x}{a}\cos\frac{m\pi y}{b}\, e^{-\alpha_{mn}z}$$

$$+ \sum_{f=0}^{\infty}\sum_{g=1}^{\infty}\frac{\alpha_{fg}g\pi}{k_{cfg}^2 b}\hat{B}_{fg}\cos\frac{f\pi x}{a}\cos\frac{g\pi y}{b}\, e^{-\alpha_{fg}z}$$

$$\hat{H}_x = \hat{K}_{oo}e^{-j\beta_{oo}z} + \sum_{m=1}^{\infty}\sum_{n=0}^{\infty}\frac{\alpha_{mn}m\pi}{k_{cmn}^2 a}\hat{A}_{mn}\cos\frac{m\pi x}{a}\cos\frac{n\pi y}{b}\, e^{-\alpha_{mn}z}$$

$$+ \sum_{f=0}^{\infty}\sum_{g=1}^{\infty}\frac{j\omega\epsilon g\pi}{k_{cfg}^2 b}\hat{B}_{fg}\cos\frac{f\pi x}{a}\cos\frac{g\pi y}{b}\, e^{-\alpha_{mn}z}$$

$$\hat{H}_y = 0 + \sum_{m=1}^{\infty}\sum_{n=0}^{\infty}\frac{-\alpha_{mn}n\pi}{k_{cmn}^2 b}\hat{A}_{mn}\sin\frac{m\pi x}{a}\sin\frac{n\pi y}{b}\, e^{-\alpha_{mn}z}$$

$$+ \sum_{f=0}^{\infty}\sum_{g=1}^{\infty}\frac{j\omega\epsilon g\pi}{k_{cfg}^2 b}\hat{B}_{fg}\sin\frac{f\pi x}{a}\sin\frac{g\pi y}{b}\, e^{-\alpha_{fg}z}$$

$$\gamma_{mn} = \alpha_{mn} + j\beta_{mn} = \sqrt{k^2 - \left(\frac{m\pi}{a}\right)^2 - \left(\frac{n\pi}{b}\right)^2} = \sqrt{k^2 - k_{cmn}^2}$$

TABLE I

ELECTROMAGNETIC FIELD EQUATIONS FOR A MIXED-WALL WAVEGUIDE

Equations shown are for total "+z propagating" portion of the field components in a mixed-wall waveguide. With appropriate sign changes, similar equations express the "-z propagating" components.

A reflector or shorting plate inserted in the waveguide
behind the monopole (Figure C-9) produces an equivalent to
the infinite array of dipoles in Figure C-5 backed by a
reflector. A set of equations analagous to those in Table I
can then be generated for the "-z propagating" field com-
ponents of the waves reflected from the shorting plate.
Summing The +z and -z directed field components in the
neighborhood of the monopole gives rise to a set of equations
of the same form as those in a conventional waveguide backed
by a shorting plate. These equations establish matching
requirements on the monopole from the shorting plate so that
the non-evanescent wave does not propagate back up the
waveguide toward the source. Since it is generally accepted
that a probe in a conventional waveguide backed by a shorting
plate can (ideally) absorb all power flowing down the wave-
guide[10], it is therefore expected that a probe (monopole) will
absorb all power flowing down a mixed-wall waveguide. Therefore

+z (Direction of
energy flow down
waveguide)

Monopole
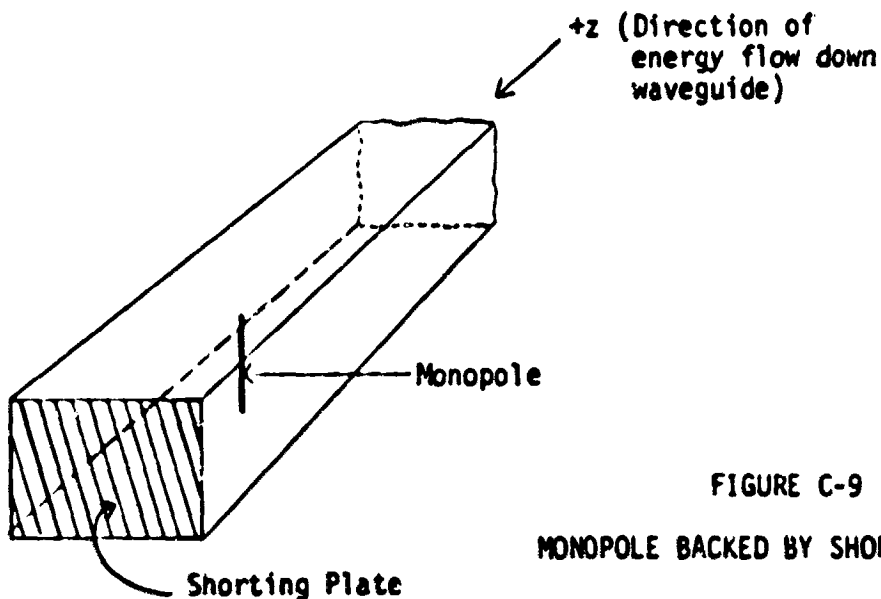
Shorting Plate

FIGURE C-9

MONOPOLE BACKED BY SHORTING PLATE

total absorption of the plane wave power beam by a dipole in a Rectenna requires that the separation between dipoles be within limits which restrict propagation in the mixed-wall waveguide to the TEM mode. A full-scale computer analysis to test this hypothesis is recommended. However, agreement of these results with those of the current sheet model and grating lobe analysis (Appendix D) convinces us that this "mixed-wall waveguide" model is properly respresentative of a Rectenna of infinite extent.

Since the waveguide dimensions which restrict propagation to the TEM mode are less than λ in the "a" direction and less than $\lambda/2$ in the "b" direction of Figures C-5 and C-6, and since the separation between the centers of the dipoles is "a" by "2b" (Figure C-7), then the maximum allowable separation of the centers of dipoles for total absorption of a plane wave, for the rectangular grid configuration of Figure C-6 (page 64) is just under one wavelength.

APPENDIX D

GRATING LOBES

Page intentionally left blank

GRATING LOBES

Three types of reradiation may be expected from the rectenna: random, specular, and grating lobe scatter. Whenever a regularly spaced array of coherent sources exists, there is a possibility of grating lobes.*

If for any systematic or non-random reason the criteria discussed elsewhere are not perfectly met and energy is therefore radiated from individual elements, it is essential that the directions in which the energy radiates be predictable.

An infinite planar array of isotropic antennas is illustrated in Figure D-1. The pattern multiplication theorem allows
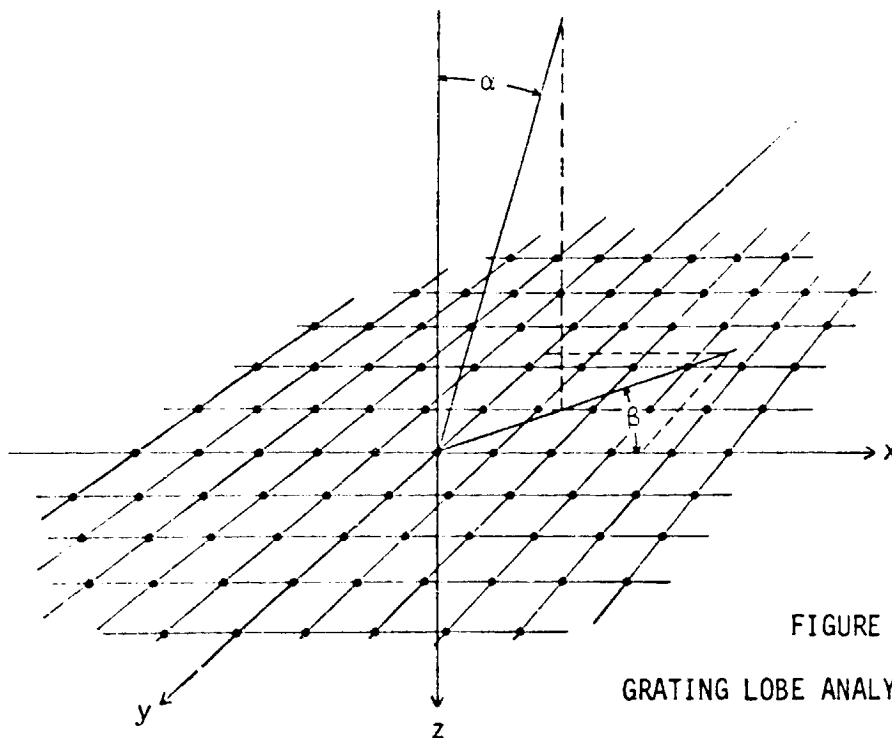
FIGURE D-1

GRATING LOBE ANALYSIS GEOMETRY

*In pre-laser optics, structures such as gratings cut in an opaque sheet were used with a single source to permit interference experiments--hence the name.

each of the isotropic elements to represent for our present purposes one dipole and its image in the reflector. Of course, any analysis based on these isotropic elements lacks any element pattern effects and, for that matter, suppresses polarization effects where present.

In Figure D-2 the angle α is restricted to the x-y plane
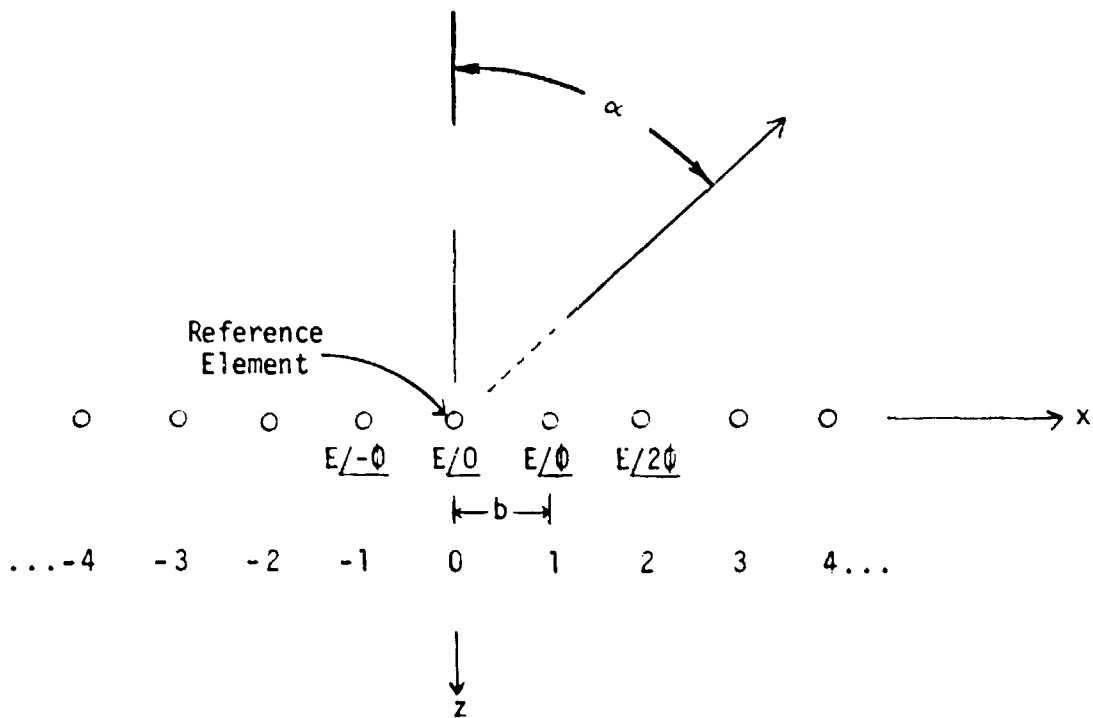
FIGURE D-2

GRATING LOBE ANALYSIS GEOMETRY (SIDE VIEW)

($\beta = 90^\circ$ in Figure D-1). The angle α is the angle at which a grating lobe, if any, will be produced if all elements are excited at the sample amplitude and with a phase variation uniformly progressive with x as shown.

Once again in anticipation of multiplication of patterns
we are letting each element in Figure D-2 represent a row
of elements along z = constant, x = constant lines.

We shall stipulate that phase will be measured relative
to the field component produced by the reference element.
If the element immediately to the right of the reference
element is excited at a leading phase ϕ, the two will generate
a signal in the α direction of

(D-1) $\qquad \hat{E}_{TOT} = E \underline{/0^O} + E \underline{/\phi + 2\pi b'\sin \alpha}$

where $b' = \dfrac{b}{\lambda}$ is the wavelength-normalized distance between
elements. For a large array with uniform phase distribution,

(D-2) $\qquad \hat{E}_{TOT} = \sum_{n=-p}^{q} E \underline{/n(\phi + 2\pi b'\sin\alpha)}$

In the limit $p \to \infty$, $q \to \infty$ Equation (D-2) tends to zero
except when

(D-3) $\qquad (n + 1)\left[\phi + 2\pi b'\sin \alpha\right] = n\left[\phi + 2\pi b'\sin \alpha\right] + 2\pi m$

(D-4) $\qquad \phi + 2\pi b'\sin \alpha = 2\pi m$ $\qquad\qquad$ m an integer

By Equation (D-4) we are stating that grating lobes will
exist in the directions

(D-5) $\qquad \alpha = \sin^{-1}\left[\dfrac{2\pi m - \phi}{2\pi b'}\right]$

This suggests that the grating lobe pattern is impulsive (i.e.,

has zero beamwidth). Mathematically,

$$\hat{E}(\theta,\beta) = \hat{A}(\beta) \, \delta(\theta - \alpha)$$

This is true only for a truly infinite array. We believe
that an analysis of the very large but finite rectenna would
show the peak of grating lobes to be at an excellent approximation
of the α direction. We are particularly interested here in
the special cases associated with excitation of the elements
by incoming signals. Figure D-3 represents the same array as
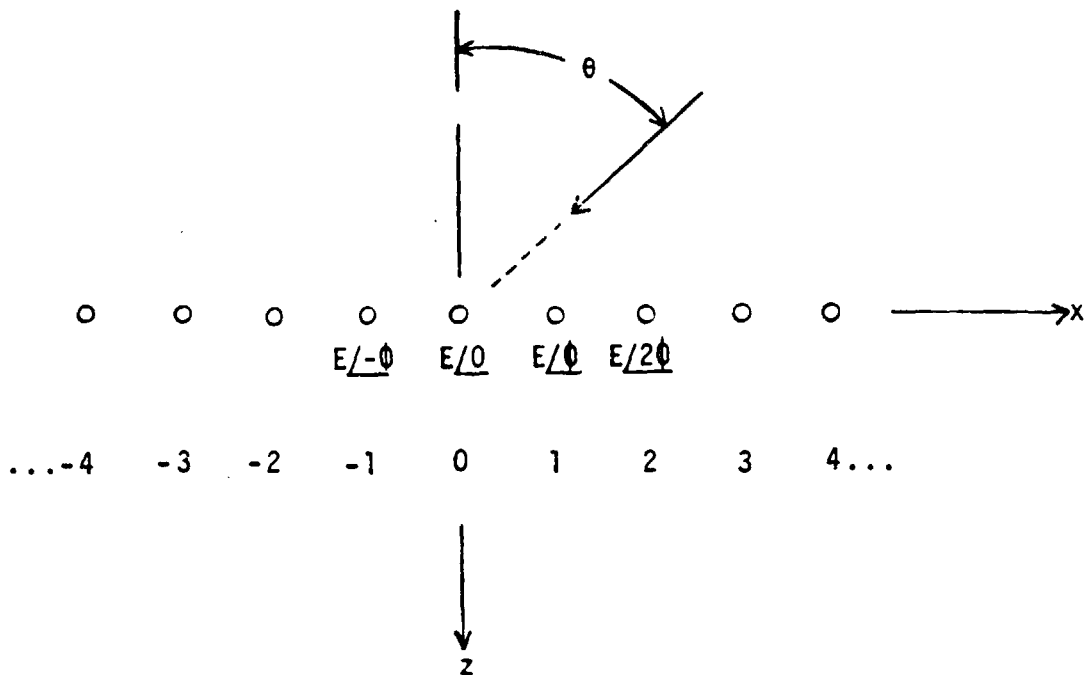
FIGURE D-3

GRATING LOBE ANALYSIS GEOMETRY
(Incoming Signals)

Figures D-1 and D-2 but with emphasis on a plane wave (compare
Appendixes A and B) incoming from an angle θ.* If we once
again stipulate that phase will be measured relative to the

---

*Note that both α and θ are colatitude angles—measured in
the x-z plane.

element at the origin, the incoming plane wave will produce currents in the elements proportional to

(D-6) $\hat{E}_n = E \underline{/2\pi n b' \sin\theta}$

That is, in Equations (D-1) and (D-2)

$$\phi = 2\pi b' \sin\theta$$

If we now insert this result into Equation (D-5) we obtain

(D-7) $\alpha = \sin^{-1}\left[\dfrac{2\pi m - 2\pi b' \sin\theta}{2\pi b'}\right]$

For m = 0

$$\alpha = \sin^{-1}\left[-\sin\theta\right]$$

$$\alpha = -\theta$$

for all b'. This is the specular reflection and not a true grating lobe even though it comes through the same mathematics. Note, too, that nothing here indicates that this will not have a zero amplitude. The true grating lobes occur for m > 0.

$$\alpha = \sin^{-1}\left[\frac{m}{b'} - \sin\theta\right]$$

and we conclude that for grating lobes to be produced b' must be such that α is real:

(D-8) $-1 \leq \dfrac{m}{b'} - \sin\theta \leq +1$

or

(D-8') $\dfrac{m}{b'} \leq 1 + \sin\theta \qquad\qquad 0 \leq \theta \leq \pi/2$

The "first" grating lobe corresponds to m ≈ 1. To avoid fundamental frequency grating lobes, we need to consider only this case.

Hence, we require

(D-9) $b' < \dfrac{1}{1 + \sin\theta}$

to avoid grating lobes.

The analysis above is quite adequate for a rectangular configuration. However, the reference rectenna has an equilateral triangular configuration such as illustrated in Figure D-4.
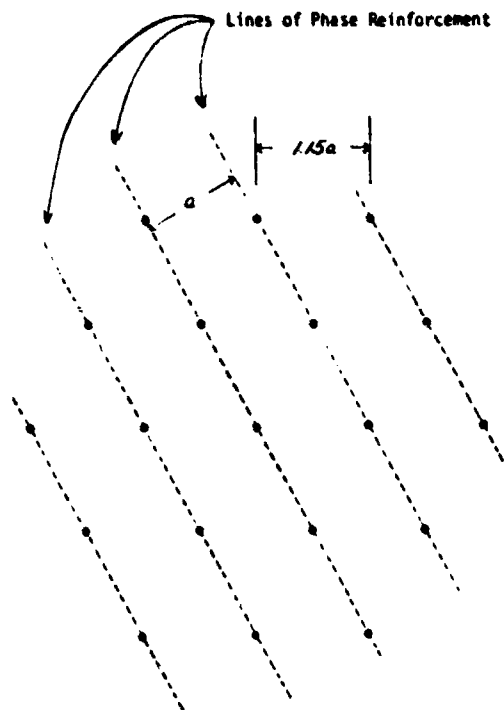
FIGURE D-4

CONFIGURATION OF REFERENCE RECTENNA

Simple trigometry tells us that the "slant" and "horizontal" separations have a 1.15 : 1 ratio for the equilateral triangles as shown.

Again invoking the concepts of pattern multiplication, we select any one side of a triangle, draw a family of lines parallel thereto, and represent the elements along each line by a single element. For the incoming signal normal to the array all (actual) elements are in phase and thus so are the fictitious elements of each line. On the basis of the earlier discussion we therefore conclude that

$$a < \lambda$$

or $\qquad\qquad 1.15a < 1.15\lambda$

provides the criterion for non-existence of grating lobes for <u>normal incidence</u>. If a terrain-conforming design as suggested elsewhere in this report is to be considered with the triangular array, a grating lobe analysis for that case should be undertaken.

Harmonic Grating Lobes

The presence of diodes close to the dipoles of the rectenna elements suggests the possible generation of harmonic currents. Because the elements are expected to be similar, the incoming signal will produce harmonics having a phase regularity. Where elements are identical, the analysis of this Appendix will be approximately applicable, failing only because of finiteness of regions. The patterns of harmonic grating lobes can be deduced by reference to analysis similar to

that associated with Equation (D-7). It should be noted, however, that as harmonics are introduced there are grating lobes in directions outside the "plane of incidence" as defined by the Poynting's vectors of the incoming and specular reflection. A full analysis for the angle of incidence not zero (i.e., the "terrain conforming" design) is beyond the scope of our present task. For the special case of $\theta = 0$, all elements are excited in phase. For a rectangular array a grating lobe can exist at any longitudinal angle for which Equation (D-7) is satisfied (for $\theta = 0$). Thus, for the second harmonic,

$$(D-10) \qquad \alpha = \sin^{-1} \frac{2\pi m}{2\pi b}"$$

$$= \sin^{-1} \frac{m}{b}"$$

where the double prime implies that separation has been normalized to the wavelength of the second harmonic (as opposed to the fundamental).

One convenient approach to the harmonic grating lobes is to assume that $b"$ is so small as to make second harmonic grating lobes impossible and then consider changes as $b"$ increases.* As $b"$ reaches unity ($b = 0.5\lambda_{fund} = \lambda_2$) four grating lobes at $\alpha = 90°$ and $\beta = 0°$, $\pm 90°$, and $180°$ come into existence. Because of the infinite extent assumption we expect harmonic grating lobes to be impulsive just

---

*Note that a rectangular array will be approximately square in order to prevent grating lobes at the fundamental.

as were the fundamental ones. Further increase in b" will cause the angle α associated with the first set to decrease. A value of b" is eventually reached which brings forth four more lobes at $\alpha = 90°$ and $\beta = \pm 45°$ and $\pm 135°$. Increasing b" beyond this point would cause these four to shift to smaller α and would eventually give rise to four more. Before this condition has been reached, of course, there would be fundamental grating lobes and this many second harmonic lobes would not be expected. However, third and fourth harmonics would produce the same type pattern. In general one would expect progressively smaller amplitudes at higher harmonics. Care must be exercised in design of the rectenna to avoid any resonances at these harmonics which might cause enhancement.

A similar pattern of harmonic grating lobes is expected for the triangular array except that six lobes spaced by 60° are to be expected for each set.

Introduction of element patterns will, of course, alter the relative amplitudes of lobes. However for harmonics it is likely that radiations would be from more than just the dipole portion. Until more is known about characteristics of individual elements, little more can be done with this aspect of the problem.

As has been noted above, an ideally arrayed rectenna

of infinite extent would produce grating lobes which are
impulsive. In general, a shift to finite extent or
introduction of typical variations in element placement
should generate more typical patterns. Both of these
departures from the ideal should eventually be examined.

APPENDIX E

TOLERANCE AND PERTURBATION ANALYSIS

TOLERANCE AND PERTURBATION ANALYSIS

An actual rectenna may deviate from the ideal for a number of reasons:

1. Random construction variations

    a. Geometrical (three displacements, three rotations)

    b. Impedance (element length or diode-load)

2. Systematic variations

    a. Impedance error

    b. Spacing error (dipole-reflector)

    c. Angular error

3. Atmospheric induced randomness

These deviations all produce "errors" in the sense of reduced efficiency and/or scattering.

Any one deviant element will scatter approximately isotropically, with amplitude and phase dependent upon the nature of the deviation. Thus, the study of random construction variations as an electromagnetic influence will need to wait for statistical quality control information as an input. Certain systematic and atmospherically induced variations can, however, be usefully anticipated at this time.

Systematic Variations

The second class of "errors" can be treated using the current sheet model (See Appendix B). Equations (B-21) and (B-34) indicate the reflected power (specularly scattered

PRECEDING PAGE BLANK NOT FILMED

component) for deviations from nominal design values, thus:

$$\text{(B-21)} \quad \rho_{\uparrow} = -\frac{(\frac{\eta}{R_o}\cos\theta - 1) + j\cot\ (\frac{2\pi}{\lambda}d\cos\theta)}{(\frac{\eta}{R_o}\cos\theta + 1) + j\cot\ (\frac{2\pi}{\lambda}d\cos\theta)}$$

$$\text{(B-34)} \quad \rho_{\rightarrow} = \frac{(\frac{\eta}{R_o}\sec\theta - 1) - j\cot\ (\frac{2\pi}{\lambda}d\cos\theta)}{(\frac{\eta}{R_o}\sec\theta + 1) - j\cot\ (\frac{2\pi}{\lambda}d\cos\theta)}$$

from which the power reflection coefficients are

$$\text{(E-1)} \quad |\rho_{\uparrow}|^2 = \frac{(\frac{\eta}{R_o}\cos\theta - 1)^2 + \cot^2\ (\frac{2\pi}{\lambda}d\cos\theta)}{(\frac{\eta}{R_o}\cos\theta + 1)^2 + \cot^2\ (\frac{2\pi}{\lambda}d\cos\theta)}$$

$$\text{(E-2)} \quad |\rho_{\rightarrow}|^2 = \frac{(\frac{\eta}{R_o}\sec\theta - 1)^2 + \cot^2\ (\frac{2\pi}{\lambda}d\cos\theta)}{(\frac{\eta}{R_o}\sec\theta + 1)^2 + \cot^2\ (\frac{2\pi}{\lambda}d\cos\theta)}$$

For the reference system case with normal incidence and with proper dipole-reflector separation

$$\text{(E-3)} \quad |\rho_{\uparrow}|^2 = |\rho_{\rightarrow}|^2 = \frac{(\frac{\eta}{R_o} - 1)^2}{(\frac{\eta}{R_o} + 1)^2} = \frac{(\frac{\eta - R_o}{R_o})^2}{(\frac{\eta + R_o}{R_o})^2} = \frac{(\eta - R_o)^2}{(\eta + R_o)^2}$$

For small excursions in R_o around the nominal value η, we can claim

$$R_o \doteq \eta$$

so that

$$\text{(E-4)} \quad |\rho_{\uparrow}|^2 = |\rho_{\rightarrow}|^2 \doteq \left[\frac{\eta - R_o}{2\eta}\right]^2$$

For normal incidence and impedance match we have

$$\text{(E-5)} \quad |\rho_{\uparrow}|^2 = |\rho_{\rightarrow}|^2 = \frac{\cot^2\ (\frac{2\pi}{\lambda}d)}{4 + \cot^2\ (\frac{2\pi}{\lambda}d)}$$

For small excursions in $\frac{d}{\lambda}$ from the normal value $\frac{d}{\lambda} = 0.25$ we can write

(E-6) $\quad |\rho_\uparrow|^2 = |\rho_\rightarrow|^2 \doteq \dfrac{\cot^2 (\frac{2\pi}{\lambda} d)}{4}$

Only in the case of angular deviation do we find it necessary to separate $\rho_\uparrow$ and $\rho_\rightarrow$. For proper dipole-reflector separation and impedance match we have

(E-7) $\quad |\rho_\uparrow|^2 = \dfrac{(\cos\theta - 1)^2 + \cot^2 (\frac{\pi}{2} \cos\theta)}{(\cos\theta + 1)^2 + \cot^2 (\frac{\pi}{2} \cos\theta)}$

(E-8) $\quad |\rho_\rightarrow|^2 = \dfrac{(\sec\theta - 1)^2 + \cot^2 (\frac{\pi}{2} \cos\theta)}{(\sec\theta + 1)^2 + \cot^2 (\frac{\pi}{2} \cos\theta)}$

For small excursions of θ from $\theta = 0$

$$\cos\theta \doteq 1 - \frac{\theta^2}{2!}$$

and

$$\sec\theta \doteq 1 + \frac{\theta^2}{2!}$$

so that

(E-9) $\quad |\rho_\uparrow|^2 \doteq |\rho_\rightarrow|^2 \doteq \dfrac{\frac{\theta^4}{4} + \cot^2 (\frac{\pi}{2} \cos\theta)}{4 + \cot^2 (\frac{\pi}{2} \cos\theta)}$

Plots of Equations (E-4), (E-6) and (E-9) are given on Page 14. It should be noted that these plots are drawn to drastically different scales and indicate that the rectenna is least sensitive to errors in angle and most sensitive to errors in dipole-reflector separation. Similar relationships can,

of course, be found for a terrain conforming rectenna design. However, shape and details depend upon the design value of θ.

The discussion above is aimed entirely at cases in which the rectenna itself deviates from the ideal in a systematic way. (The angular error, of course, could also be associated with satellite drift from station). We must also recognize the possibility of the incoming signal varying from the assumed approximation of a plane wave.

"Random Signal" Errors

Wait's work[7,8] strongly supports the current sheet model as adequate for phenomena observable at a reasonable distance from the Rectenna. Our conclusion from that model was that 100% absorption of incident energy from any prescribed direction is possible provided the angle is known and fixed, the absorber sheet impedance and separation from the reflector are appropriate for the angle, and the incoming signal is a uniform plane wave. We feel that these conditions can be adequately approximated in the average to provide significant encouragement. However, there are possible external conditions which can cause deviation from these requirements. It is our intent here to point out some of these conditions. To provide insight into the problem, let us first reconsider the current sheet model, but this time with the incident signal non-uniform. This incident signal can be decomposed into two components: the uniform illumination originally posited plus a deviation signal. Using the parallel

polarization case as an example we write (following Equation (A-12))

$$(E-10) \quad \hat{\underline{E}}_1 = (\underline{u}_x \cos\theta - \underline{u}_z \sin\theta) \, \hat{A}_+ e^{-jk(x\sin\theta + z\cos\theta)} + \hat{\underline{\Xi}}$$

where the $\hat{A}_+$ component is the expected uniform illumination and $\hat{\underline{\Xi}}$ is the deviation. If the entire system is assumed to be linear*, the response can be described as the sum of the responses to the $\hat{A}_+$ and $\hat{\underline{\Xi}}$ components found individually. When the conditions of Equations (B-41) and (B-42) are met, the reflected component due to A_+ is, of course, zero. A repetition of the derivation for the current sheet model using $\hat{\underline{\Xi}}$ as input will yield, with effort, the scatter due to $\hat{\underline{\Xi}}$.

Evaluation of expected $\hat{\underline{\Xi}}$ functions will require experimental inputs. However, we can gain considerable insight into the problem by examining the disturbance to (reflection from) the linear current sheet model caused by a point source at a general disturbance point (x_0, y_0, z_0) (See Figure E-1). Once we can establish the error signal at an observation point (x,y,z) due to a point source we will be able to determine the result of any specified disturbance by representing it by a continuum of point sources.

To analyze the result of a point source we will use the current sheet model. Previously, we found it convenient to treat the two reflecting surfaces together. For our

_____

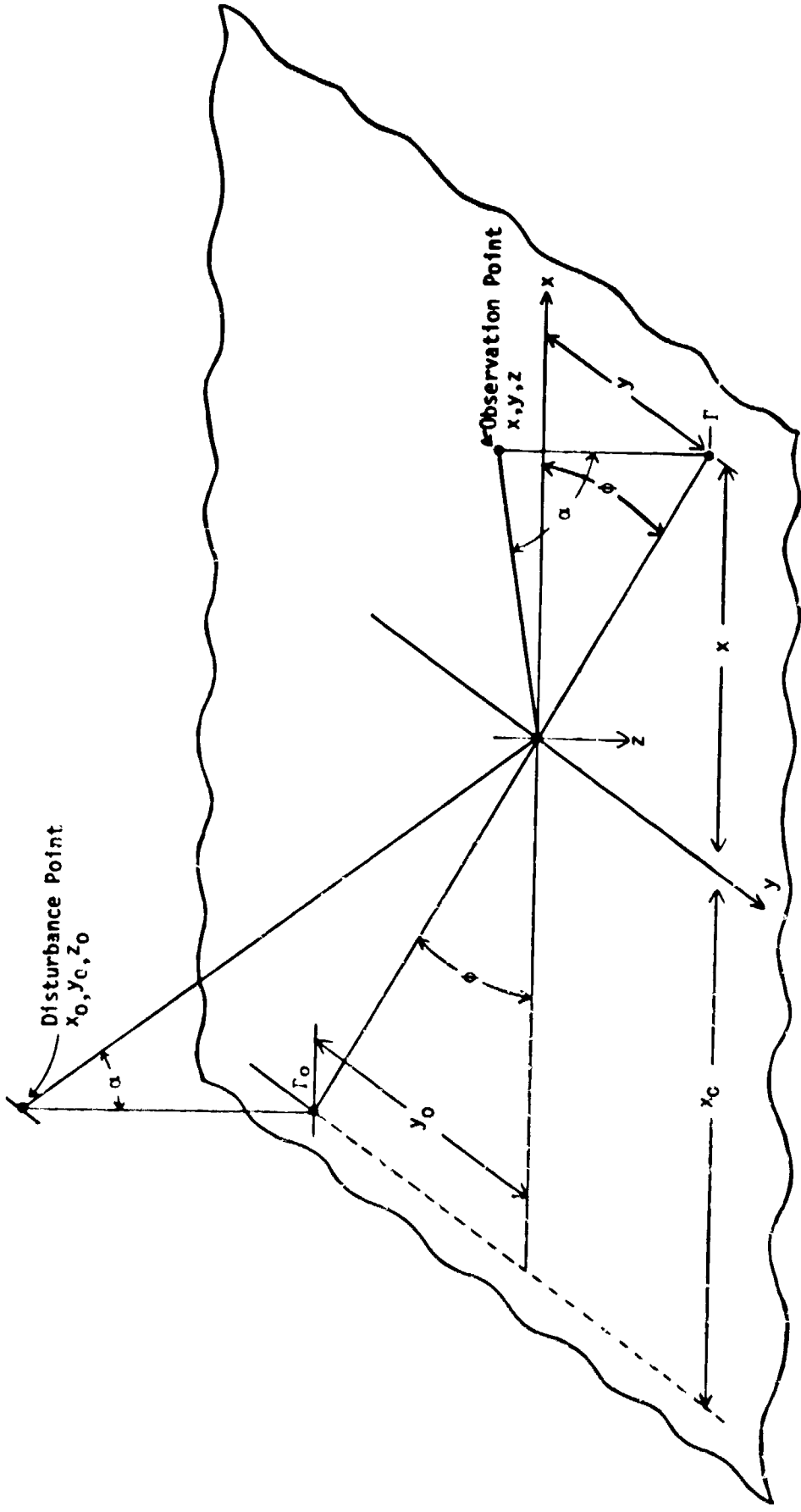*The question of linearity is not trivial. See discussion on page 30.

FIGURE E-1

PERTURBATION ANALYSIS GEOMETRY

present purposes we choose to treat the surfaces separately.
Consider a plane wave such as is described by Equations (A-12)
and (A-13) impinging on a conductive, infinitessimally thin
sheet dividing two semi-infinite regions (See Figure E-2).
Note that the properties on either side of the conductive sheet
are assumed identical so that $\alpha_1 = \alpha_2 = \alpha$.

PARALLEL POLARIZATION

For Region 1 (z < 0):

(E-11) $\hat{\underline{E}}_1 = (\underline{u}_x \cos \alpha - \underline{u}_z \sin \alpha) \; \hat{M}_\uparrow e^{-jk(x\sin \alpha + z \cos \alpha)}$

$+ (\underline{u}_x \cos \alpha + \underline{u}_z \sin \alpha) \; \hat{N}_\uparrow e^{-jk(x \sin \alpha - z \cos \alpha)}$

(E-12) $\hat{\underline{H}}_1 = \underline{u}_y \; \eta^{-1} \; [\hat{M}_\uparrow e^{-jk(x \sin \alpha + z \cos \alpha)}$

$-\hat{N}_\uparrow e^{-j(x \sin \alpha - z \cos \alpha)}]$

Similarly, for Region 2 (0 < z):

(E-13) $\hat{\underline{E}}_2 = (\underline{u}_x \cos \alpha - \underline{u}_z \sin \alpha) \; \hat{P}_\uparrow e^{-jk(x \sin \alpha + z \cos \alpha)}$

(E-14) $\hat{\underline{H}}_2 = \underline{u}_y \; \eta^{-1} \; \hat{P}_\uparrow e^{-jk(x \sin \alpha + z \cos \alpha)}$

Now at z = 0 we have the very thin sheet of high but finite
conductivity shown in Figure B-3 (Page 50). We have already
shown that at such a surface

(B-17) $\hat{H}_{1t} - \hat{H}_{2t} = \dfrac{E_t(0)}{R_o}$
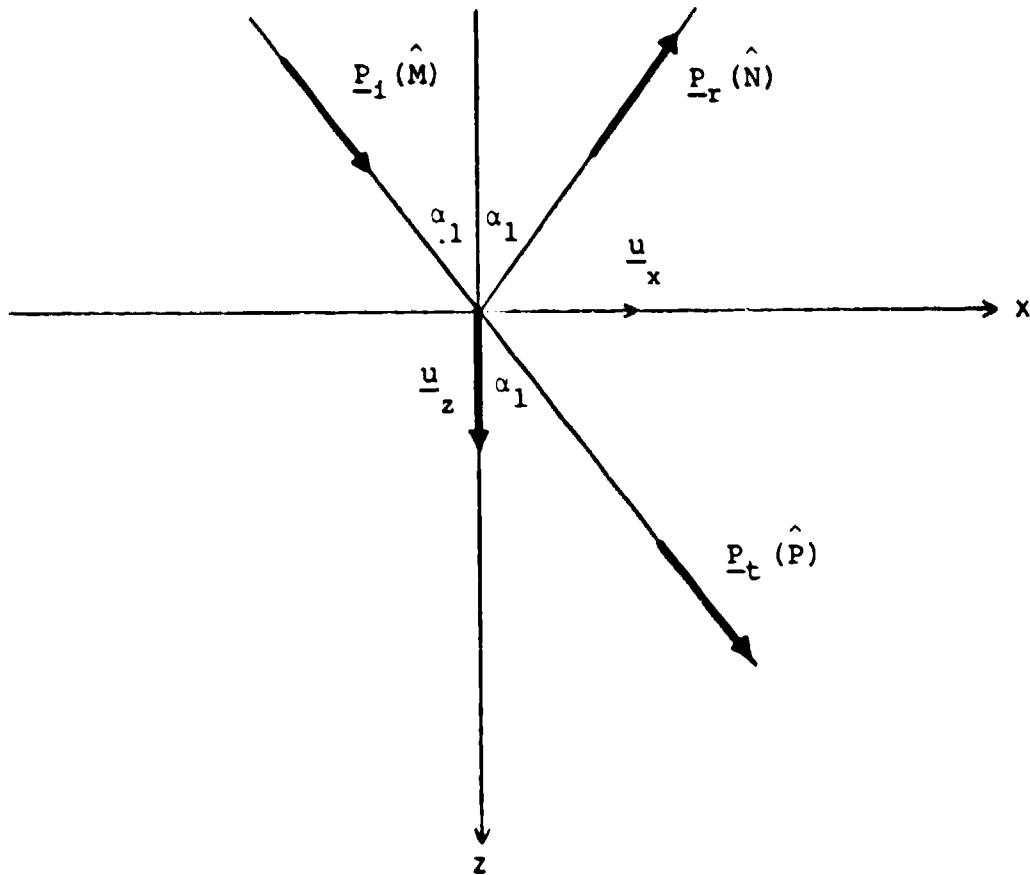
FIGURE E-2

REFLECTION GEOMETRY

Examining the tangential components at z = 0 gives us

(E-15) $\hat{E}$: $\underline{u}_x \cos \alpha (\hat{M}_\uparrow + \hat{N}_\uparrow) e^{-jkx \sin \alpha}$

$$- \underline{u}_x \cos \alpha \, \hat{P}_\uparrow e^{-jkx \sin \alpha} \quad \underset{\equiv}{x,y} \; 0$$

(E-16) $\hat{M}_\uparrow + \hat{N}_\uparrow = \hat{P}_\uparrow$

(E-17)   H: $\underline{u}_y \eta^{-1} \left[(\hat{M}_\uparrow - \hat{N}_\uparrow) e^{-jkx \sin \alpha} - \hat{P}_\uparrow e^{-jkx \sin \alpha} \right]$

$$\underset{\equiv}{x,y} \quad \underline{u}_y \cos \alpha \frac{\hat{P}_\uparrow}{R_o} e^{-jkx \sin \alpha}$$

From Equation (E-17) we obtain

(E-18) $\hat{M}_\uparrow - \hat{N}_\uparrow = \hat{P}_\uparrow \left[1 + \frac{\eta}{R_o} \cos \alpha \right]$

into which we substitute Equation (E-16) to obtain

(E-19) $\hat{M}_\uparrow - \hat{N}_\uparrow = (\hat{M}_\uparrow + \hat{N}_\uparrow) \left[1 + \frac{\eta}{R_o} \cos \alpha \right]$

from which

(E-20) $r_\uparrow = \dfrac{\hat{N}_\uparrow}{\hat{M}_\uparrow} = - \dfrac{\dfrac{\eta}{R_o} \cos \alpha}{2 + \dfrac{\eta}{R_o} \cos \alpha}$

$$= - \frac{\cos \alpha}{2 R_o' + \cos \alpha}$$

where $R_o' \equiv \dfrac{R_o}{\eta}$ is the normalized resistance of the sheet.

Returning to Equation (E-16) we obtain

$$(E\text{-}21) \quad \hat{P}_\uparrow = \hat{M}_\uparrow \left[1 - \frac{\cos \alpha}{2\ R_o' + \cos \alpha} \right]$$

$$(E\text{-}22) \quad t_\uparrow = \frac{\hat{P}_\uparrow}{\hat{M}_\uparrow} = \frac{2R_o'}{2R_o' + \cos \alpha}$$

It is almost, but not quite, trivial to extend this analysis to the ideal reflector $(\sigma \to \infty,\ R_o' \to 0)$.

$$(E\text{-}20') \quad \lim_{\sigma \to \infty} t_\uparrow = -1$$

That is, we experience full reflection with 180° phase shift. Note that this is the same result given as Equation (C-9).

PERPENDICULAR POLARIZATION

We will now apply essentially the same approach to the perpendicular polarization case. For Region 1 $(z < 0)$:

$$(E\text{-}23) \quad \hat{\underline{E}}_1 = \underline{u}_y \left[\hat{M}_\to e^{-jk(x \sin \alpha + z \cos \alpha)} - \hat{N}_\to e^{-jk(x \sin \alpha - z \cos \alpha)} \right]$$

$$(E\text{-}24) \quad \hat{\underline{H}}_1 = \eta^{-1} \left[(-\underline{u}_x \cos \alpha + \underline{u}_z \sin \alpha)\ \hat{M}_\to e^{-jk(x \sin \alpha + z \cos \alpha)} \right.$$
$$\left. + (-\underline{u}_x \cos \alpha - \underline{u}_z \sin \alpha)\ \hat{N}_\to e^{-jk(x \sin \alpha + z \cos \alpha)} \right]$$

For Region 2 $(0 < z)$:

$$(E\text{-}25) \quad \hat{\underline{E}}_2 = \underline{u}_y\ \hat{P}_\to e^{-jk(x \sin \alpha + z \cos \alpha)}$$

$$(E\text{-}26) \quad \hat{\underline{H}}_2 = \eta^{-1}(-\underline{u}_x \cos \alpha + \underline{u}_x \sin \alpha)\ \hat{P}_\to e^{-jk(x \sin \alpha + z \cos \alpha)}$$

As before,

(B-29) $\hat{H}_{1t} - \hat{H}_{2t} = \dfrac{-\hat{E}_t(0)}{R_0}$

(E-27) $\qquad\qquad = -\dfrac{\hat{P}_\rightarrow}{R_0}\, e^{-jkx\sin\alpha}$

Examining tangential components at z = 0 gives us

(E-28) $\hat{\underline{E}}$: $\underline{u}_y\,[\hat{M}_\uparrow - \hat{N}_\uparrow]e^{-jkx\sin\alpha} - \underline{u}_y\,\hat{P}_\rightarrow e^{-jkx\sin\alpha}\quad {x,y \atop \equiv}\ 0$

(E-29) $\hat{M}_\rightarrow - \hat{N}_\rightarrow = \hat{P}_\rightarrow$.

(E-30) $\hat{\underline{H}}$: $-\underline{u}_x\,\eta^{-1}\,(\hat{M}_\rightarrow + \hat{N}_\rightarrow)\cos\alpha\,e^{-jkx\sin\alpha}$

$\qquad\qquad\qquad + \underline{u}_x\,\eta^{-1}\,\hat{P}_\rightarrow\cos\alpha\,e^{-jkx\sin\alpha}$

$\qquad\qquad\qquad\quad {x,y \atop \equiv}\ -\underline{u}_x\,\dfrac{\hat{P}_\rightarrow}{R_0}\,e^{-jkx\sin\alpha}$

(E-31) $(\hat{M}_\rightarrow + \hat{N}_\rightarrow)\cos\alpha = \hat{P}_\rightarrow\left[\cos\alpha + \dfrac{\eta}{R_0}\right]$

(E-32) $\hat{M}_\rightarrow + \hat{N}_\rightarrow = \hat{P}_\rightarrow\,(1 + \dfrac{\eta}{R_0\,\cos\alpha})$

$\qquad\qquad = (\hat{M}_\rightarrow - \hat{N}_\rightarrow)\,(1 + \dfrac{1}{R_0'\,\cos\alpha})$

$\qquad\qquad \hat{N}_\rightarrow\,(1 + 1 + \dfrac{1}{R_0'\,\cos\alpha}) = \hat{M}_\rightarrow\,(1 + \dfrac{1}{R_0\,\cos\alpha} - 1)$

(E-33) $\hbar_\rightarrow = \dfrac{\hat{N}_\rightarrow}{\hat{M}_\rightarrow} = \dfrac{1}{2R_0'\,\cos\alpha + 1}$

(E-34) $\ell_\rightarrow = \dfrac{\hat{P}_\rightarrow}{\hat{M}_\rightarrow} = \dfrac{2R_0'\,\cos\alpha}{2R_0'\,\cos\alpha + 1}$

For the ideal reflector

(E-35) $\lim_{\sigma \to 0} \lambda_{+} = 1$

telling us that we have full reflection without any phase shift.

Although the results for reflection and transmission co-
efficients are polarization sensitive, we recognize that many
aspects of our problem are not. Consider the geometry shown
in Figure E-3. Here we treat a scattering point source located
at x_0, y_0, z_0 and wish to determine the resulting disturbance
at an observation point x, y, z. We will require that the slant
range from each of these points to the reflecting surfaces
be sufficiently large to allow us to visualize local disturbances
at the reflectors as plane waves. (Figure E-3 is a view of
the cross-section seen along the $\Gamma_0 - \Gamma$ line of Figure E-1.)
From the disturbance point energy may reach the observation
point by several "reflection paths" in addition to a direct
path in which we have no present interest. These paths corre-
spond in Figure E-3 to $\alpha_0, \alpha_1, \alpha_2 \ldots$. Thus the electric field
received at x, y, z will be

(E-36) $\hat{E} = \hat{K} \left\{ M(\alpha_0) + \left[t(\alpha_1) \right]^2 e^{-j2kd \cos \alpha_1} \right.$

$\pm \left[t(\alpha_2) \right]^2 \left[\lambda(\alpha_2) \right] e^{-j4kd \cos \alpha_2}$

$\pm \left[t(\alpha_3) \right]^2 \left[\lambda(\alpha_3) \right]^2 e^{-j6kd \cos \alpha_3}$

$\pm \left[t(\alpha_4) \right]^2 \left[\lambda(\alpha_4) \right]^3 e^{-j8kd \cos \alpha_4}$
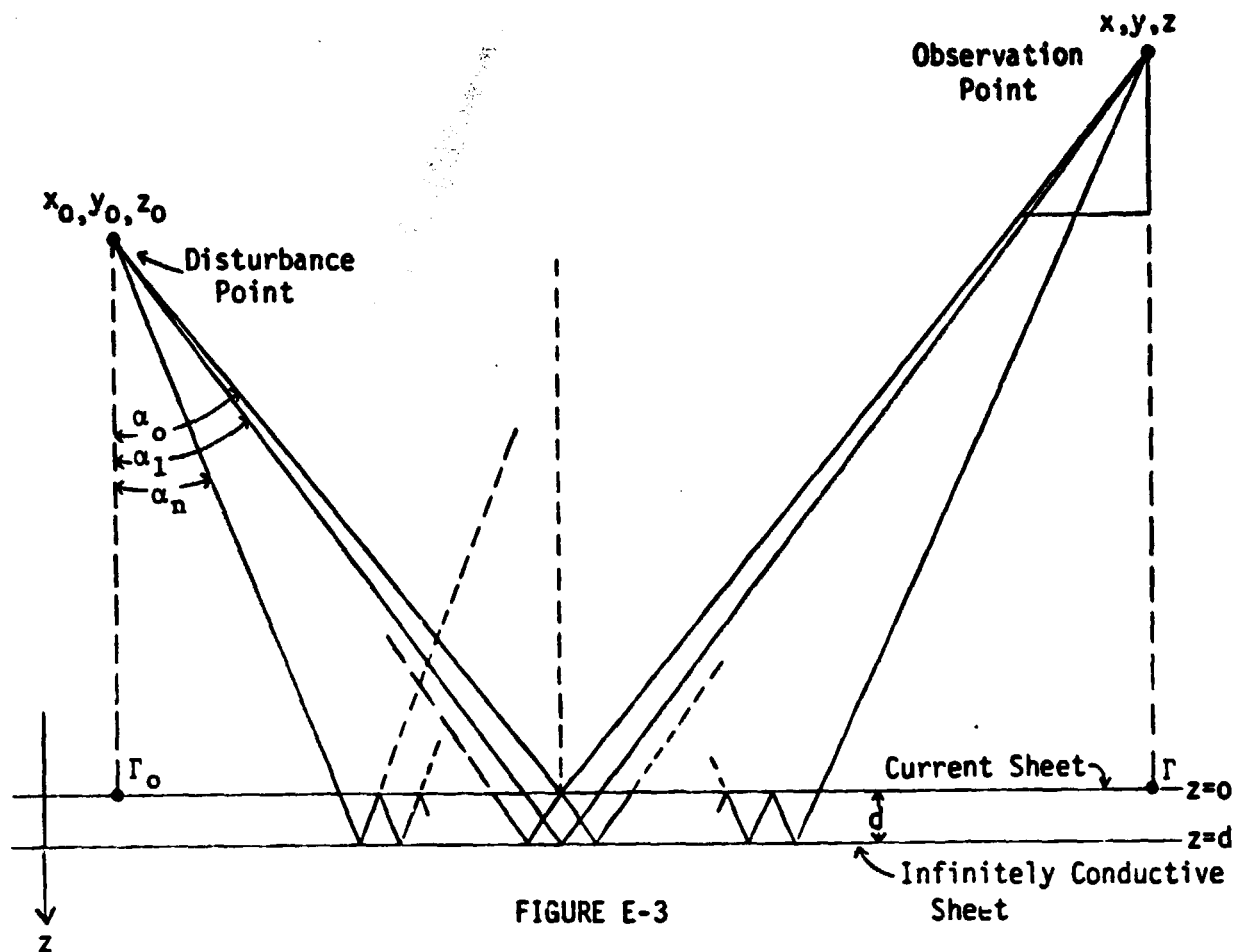
$\left. \pm \ldots \right\}$

FIGURE E-3

MULTIPLE REFLECTION GEOMETRY

where $\hat{\underline{K}}$ is both a complex (phasor) quantity and a vector
quantity serving as a normalizing coefficient which includes
the range factor (assumed to be the same for all paths).
The $\pm$ choices depend upon the polarization. To illustrate
the application of these relationships, let the point x_o, y_o, z_o,
recede such that

$$\alpha_o = \alpha_1 = \alpha_2 = \ldots$$

(i.e., x_o, y_o, z_o, are very large), and choose α to be a design
choice for perpendicular polarization. That is (from
Equations (B-41) and (B-43)),

$$d = \frac{\lambda}{4} \sec \theta \qquad\qquad (n = 1 \text{ was chosen})$$

$$= \frac{\lambda}{4} \sec \alpha$$

$$R_o = \eta \sec \theta$$

$$= \eta \sec \alpha$$

and so,

$$\mathcal{R}_{\rightarrow} = \frac{1}{2 \sec \alpha \cos \alpha + 1} = \frac{1}{3}$$

and

$$t_{\rightarrow} = \frac{2}{2 + 1} = \frac{2}{3}$$

for the design polarization (horizontal).
Thus

$$\hat{\underline{E}} = \hat{\underline{K}} \left\{ \frac{1}{3} - \left[\frac{2}{3}\right]^2 + \left[\frac{2}{3}\right]^2 \left[\frac{1}{3}\right] - \left[\frac{2}{3}\right]^2 \left[\frac{1}{3}\right]^2 \right.$$

$$\left. + \left[\frac{2}{3}\right]^2 \left[\frac{1}{3}\right]^3 - \left[\frac{2}{3}\right]^2 \left[\frac{1}{3}\right]^4 + \ldots \right\}$$

$$= \underline{K} \left\{ \frac{1}{3} - \left(\frac{2}{3}\right)^2 \sum_{q=1}^{\infty} \left(-\frac{1}{3}\right)^q \right\}$$

$$= 0$$

as the design criteria predict.

Equations (E-36), then, yield the outputs at an observation point due to point sources of the two polarizations. Within the limitations imposed by non-linearities, any source of interest can be formulated in terms of a continuum of these

point sources. This task should be well within the capability
of a computer. Thus we feel confident that we can evaluate the
scatter associated with non-uniformity due to a mis-pointed
or mal-formed power beam or due to atmospheric scatter,
provided the non-uniformity arrives at an angle such that the
current sheet model is valid. The last restriction will
disallow signals arriving at angles α large enough to generate
grating lobes.

APPENDIX F

TROPOSPHERIC/IONOSPHERIC TRANSMISSION TESTS

TROPOSPHERIC/IONOSPHERIC TRANSMISSION TESTS

OBJECTIVES

The literature[20,21] suggests that certain ionospheric and/or tropospheric phenomena will cause amplitude and phase variations in the SPS power beam as "seen" by the Rectenna. The tests described here are designed to evaluate the magnitude, type, and frequency of occurence of such effects.

Tests are particularly needed (see page 29) to determine the degree of deviation in propagation phenomena observed under two conditions unique to the SPS: monochromaticity and smallness of the effective aperture of individual Rectenna element dipoles. A search of the available literature has revealed no experimental results in which these conditions are present. Of particular interest are the amplitude and phase variations produced by the troposphere and the ionosphere.

APPARATUS

The four tests recommended here will require:

1. A transponding GEO satellite operating as closely
   as can be arranged to 2.45 GHz.*

---

*Conventional C-Band communication satellite frequencies would be acceptable.

PRECEDING PAGE BLANK NOT FILMED

2. Two conventional microwave receiving stations (the antennas for these should have apertures as small as possible consistent with acceptable signal-noise ratios);

3. Two microwave transmitters with antennas.

4. One very small aperture antenna ($\sim 1\lambda^2$);

5. One large aperture antenna ($> 1200\lambda^2$);

TEST NUMBER 1

PHASE PERTURBATION TEST

PURPOSE

To measure the extent to which spatial phase perturbations will cause the incoming signal to deviate from the desired plane wave. These measurements will provide an evaluation of this effect for monochromatic signals.

PROCEDURE

Two receiving stations are set up approximately 500 meters apart (Figure F-1). Variations in the phase differences are then measured under the conditions given below.
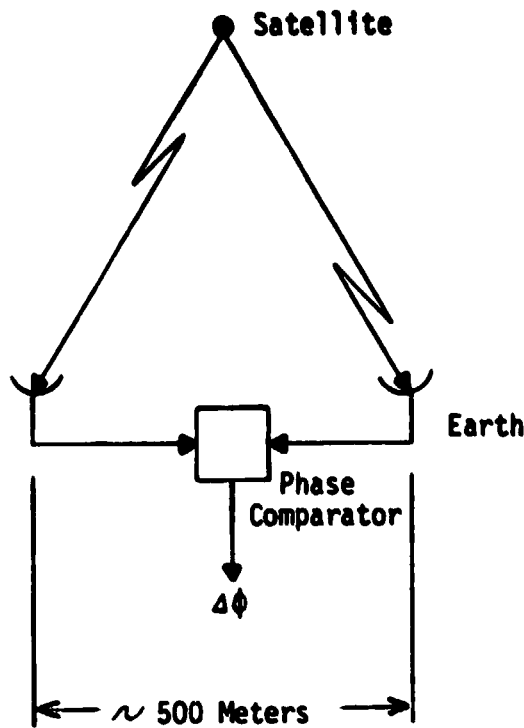
FIGURE F-1

PHASE PERTURBATION TEST

TEST NUMBER 2

AMPLITUDE FLUCTUATION TEST: SMALL/LARGE APERTURE COMPARISON

(MONOCHROMATIC)

PURPOSE

To compare amplitude fluctuations of Space-to-Earth signals received with and without the aperture averaging associated with large (high gain) receiving antennas

(see Crane and Blood[19]). While it would be desirable to perform this experiment on a Space-to-Earth link, it seems unlikely that enough power can be obtained from the satellite to provide adequate signal-to-noise ratio at the very small ($\sim 1\lambda^2$) aperture needed to properly model the Rectenna element. Since the purpose here is experimental evaluation of scintillation effects of monochromatic signals on small
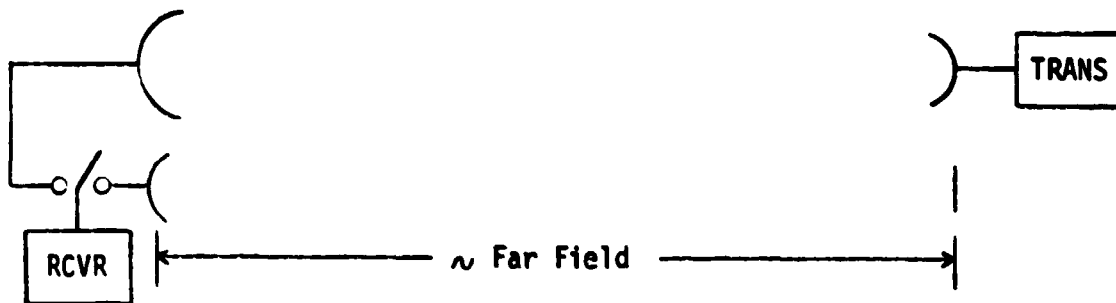
RCVR

TRANS

$\sim$ Far Field

FIGURE F-2

AMPLITUDE FLUCTUATION TEST

aperture antennas, useful insights can be obtained by comparing horizontal path measurements with those from a larger antenna.

PROCEDURE

The measurements require a conventional microwave receiver capable of being switched between a large-aperture

($\sim 1200\lambda^2$) and a small aperture ($\sim 1\lambda^2$) antenna. (Figure F-2).
Both antennas should be oriented to receive the transmission
of a single, monochromatic transmitter over as nearly the
same horizontal path as possible. The horizontal path should
be chosen to provide a wide variation of atmospheric tur-
bulence due to surface heating in a region of the far field of
both transmit and receive antennas. The receiver is switched
alternately between the antennas to provide amplitude
fluctuation statistics for a variety of measurement periods
ranging from cool, stable (e.g., early morning) to highly
turbulent (e.g., summer afternoon) conditions as well as
rain and snow conditions. Simultaneous switching of trans-
mitter power and receiver antennas will eliminate the
influence of the antennas' ideal gains.

INTERPRETATION

These measurements will indicate the degree to which
the large body of available data, taken with relatively
large antennas, is or is not applicable to the rectenna
with its virtually independent elements.

TEST NUMBER 3

AMPLITUDE FLUCTUATION TEST: MONOCHROMATIC/WIDE BAND COMPARISON

PURPOSE

To compare amplitude fluctuations of space-to-earth
signals which are 1) monochromatic and 2) modulated to

a bandwidth on the order of 30MHz to indicate the degree
to which the large body of available data, taken with
modulated signals, is or is not applicable to the mono-
chromatic transmission proposed for the SPS.

PROCEDURE

Using a conventional microwave receiver, record amplitude-
time data from satellite transmissions which alternate
between monochromatic and wide-band modulation.

TEST NUMBER 4

UP-LINK MULTI-PATH PHASE STABILITY

PURPOSE

To measure path-length phase-shifts between two up-link
signals by attempting to maintain constant phase between
them at the GEO satellite transponding antenna.

The ability to maintain a stable amplitude at the
satellite would help confirm the feasibility of the retro-
directive pilot-beam concept. Changes in phase of the
transmitted (up-link) signals needed to maintain constant
phase would indicate the magnitude of iono/tropospheric
effects on the combined signals received at the satellite.

PROCEDURE

Signals from a pair of microwave transmitters are
received in the input antenna of a single transponder aboard
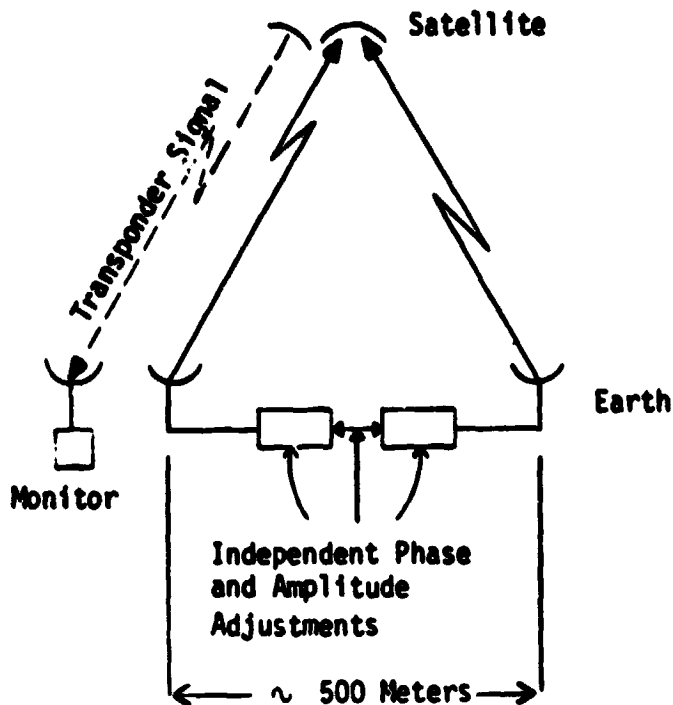
FIGURE F-3

UP-LINK MULTIPATH PHASE STABILITY TEST

the satellite. The output of this transponder, frequency shifted
but with amplitude proportional[*] to the phasor sum of the signals
received by it, is transmitted to a ground-based receiver
(Figure F-3).

The two transmissions will form an interference pattern in
space in the vicinity of the satellite (see Figure F-4). If
the phase lengths are stable, this pattern will also be stable.

With amplitudes adjusted to produce a deep null, the pattern
is shifted to place the satellite at approximately 50% of the
maximum signal strength--a position of high slope and hence,

*This requies that the combined amplitudes of the transmitters
as received at the transponder be below the transponder's
limiter threshhold.

sensitivity to shift in pattern. Amplitude shifts at the satellite (relayed over the transponder link) are a measure of differential phase shifts in the up-link paths.
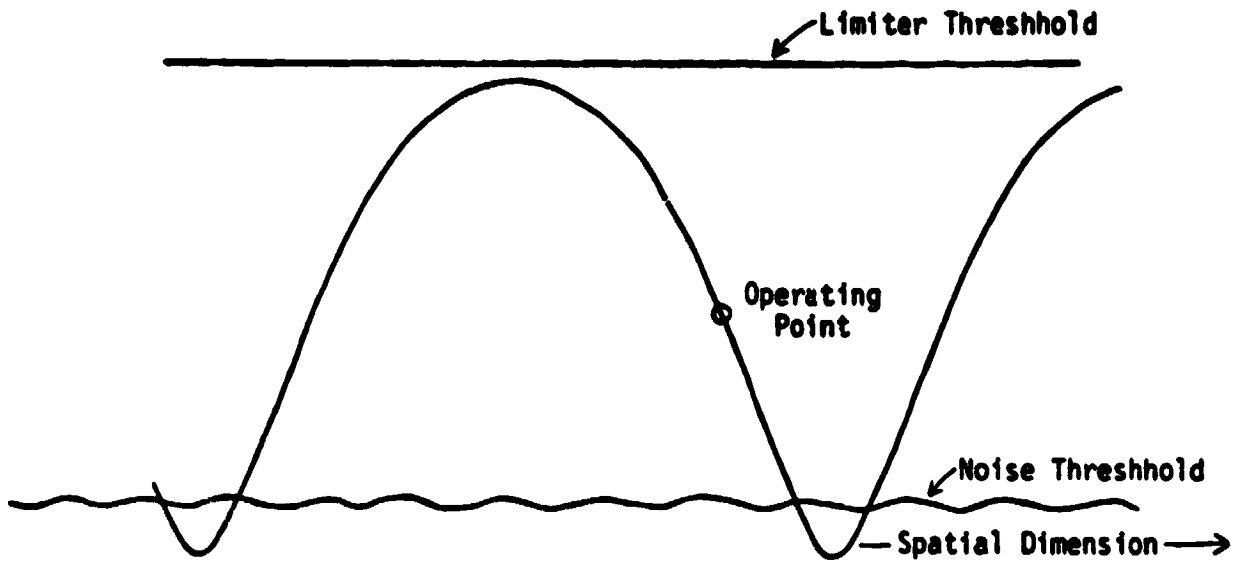

FIGURE F-4

INTERFERENCE PATTERN

GENERAL TEST CONDITIONS

The recommended tests should be performed over a period of time sufficient to observe effects not only at dusk and dawn but also of weather, especially severe storms; the effects of aircraft flying through the up- and down-links; the effects of ionospheric heating by ground-based transmitters; and the effects of unanticipated causes. Some of these tests should be extended to measure any seasonal variations (e.g., summer-fall).